Geosci. Model Dev. Discuss., https://doi.org/10.5194/gmd-2018-191
Manuscript under review for journal Geosci. Model Dev.
Discussion started: 23 August 2018

Geoscientific Model Development Discussions
Open Access
EGU

CSIB v1: a sea-ice biogeochemical model for the NEMO community ocean modelling framework

Hakase Hayashida[1], James R. Christian[2,1], Amber M. Holdsworth[2], Xianmin Hu[3], Adam H. Monahan[1], Eric Mortenson[1], Paul G. Myers[4], Olivier G. J. Riche[2], Tessa Sou[2], and Nadja S. Steiner[2,1]

[1]School of Earth and Ocean Sciences, University of Victoria, Victoria, British Columbia, Canada
[2]Fisheries and Oceans Canada, Institute of Ocean Sciences, Sidney, British Columbia, Canada
[3]Fisheries and Oceans Canada, Bedford Institute of Oceanography, Dartmouth, Nova Scotia, Canada
[4]Department of Earth and Atmospheric Sciences, University of Alberta, Edmonton, Alberta, Canada

Correspondence to: Hakase Hayashida (hakasehayashida@gmail.com)

Abstract. Numerical models are a useful tool for studying marine ecosystems and associated biogeochemical processes in ice-covered regions where observations are scarce. To this end, CSIB v1 (Canadian Sea-ice Biogeochemistry version 1), a new sea-ice biogeochemical model has been developed and embedded into the Nucleus for European Modelling of the Ocean (NEMO) modelling system. This model consists of a three-compartment (ice algae, nitrate, and ammonium) sea-ice ecosystem and a two-compartment (dimethylsulfoniopropionate and dimethylsulfide) sea-ice sulfur cycle which are coupled to pelagic ecosystem and sulfur-cycle models at the sea ice-ocean interface. In addition to biological and chemical sources and sinks, the model simulates the horizontal transport of biogeochemical state variables within sea ice through a one-way coupling to a dynamic-thermodynamic sea-ice model (LIM2). This paper describes technical aspects of implementing sea-ice biogeochemistry into NEMO and provides discussion on the results of several model experiments. Results of the reference simulation were evaluated by comparing the model outputs to observations and previous modelling studies. Additional simulations were conducted to assess the model sensitivity to 1) the temporal resolution of the snowfall forcing data, 2) the representation of light penetration through snow, 3) advective and eddy-diffusive horizontal transport of sea-ice biogeochemical state variables, and 4) light attenuation by ice algae. The sea-ice biogeochemical model has been developed within the generic framework of NEMO to facilitate its use within different configurations and domains, and can be adapted for use with other NEMO-based submodels such as LIM3 and PISCES.

1 Introduction

Biogeochemical processes at the sea ice-ocean interface play an active role in polar marine ecosystems and global cycling of important chemical elements and compounds. For example, microalgae that heavily colonize the base of sea ice in spring can have a strong influence on the primary production of underlying phytoplankton through light attenuation, nutrient drawdown,

Geosci. Model Dev. Discuss., https://doi.org/10.5194/gmd-2018-191
Manuscript under review for journal Geosci. Model Dev.
Discussion started: 23 August 2018

and seeding as well as on the secondary production by being the food source for pelagic and benthic grazers (Arrigo, 2014). Furthermore, these ecological processes regulate the production and removal of greenhouse gases (e.g. carbon dioxide and nitrous oxide) and other climatically-important gases (e.g. dimethylsulfide) in ice-covered regions and the exchange of these gases with the overlying atmosphere (Vancoppenolle et al., 2013).

However, our current understanding of many of these processes remains limited due to both logistical and technical challenges for field observations (Miller et al., 2015). Mechanistic models representing sea-ice biogeochemistry can both fill gaps between sparse measurements and aid in the interpretation of these measurements. Furthermore, these models can be used in systematic intercomparisons that can build confidence in our understanding of polar marine science such as has been done for pelagic ecosystem models (e.g. Popova et al., 2012; Jin et al., 2015).

Although considerable effort has been invested in developing mechanistic models for sea-ice bigeochemistry over the last three decades following the pioneering work of Arrigo et al. (1991), most of these models were applied in one-dimensional (1D) framework and the results are therefore applicable only to a particular location of interest (see Vancoppenolle and Tedesco, 2016). Only a few of these models have been applied in three-dimensional (3D) framework coupled to either a regional or global sea ice-ocean general circulation model (see Table 1 for a list of 3D model configurations developed for pan-Arctic studies). More efforts toward developing such 3D sea-ice biogeochemical models are needed to better understand the large-scale variability in biogeochemical processes within sea ice and their role in underlying pelagic and benthic ecosystems.

In this study, we present CSIB v1 (Canadian Sea-Ice Biogeochemistry version 1), a new sea-ice biogeochemical model implemented into the Nucleus for European Modelling of the Ocean (NEMO), a state-of-the-art modelling framework for oceanographic research (www.nemo-ocean.eu). To the best of our knowledge, Tedesco et al. (2017) is the only previous study in which a sea-ice biogeochemical model has been coupled to NEMO. However, the coupling was done in an offline configuration in that study. An important advance of the present study is that the model is written within the NEMO code to allow in-line coupling (i.e. physical dynamics are computed simultaneously with biogeochemistry) and the computation of the horizontal transport of sea-ice biogeochemical state variables. These implementations allow more realistic simulation of sea-ice biogeochemistry. The main objectives of the present study are to: describe the development of the coupled model in a pan-Arctic configuration (Section 2); evaluate the results of a multi-year reference simulation (Section 3); and assess the model sensitivity to modifications of parameters and parameterizations (Section 4). Key findings of the present study are summarized in Section 5.

2 Model description and setup

The fundamental constituents of NEMO are the following three submodels: ocean physics, sea-ice physics, and ocean biogeochemistry. In the present study, we adopted version 3.4 of NEMO (NEMO v3.4; Madec, 2008) and developed within it an additional submodel, sea-ice biogeochemistry. Technical details on the code structure of the model developed in this study are provided in Appendix A for those who are interested in using the newly-added sea-ice biogeochemical model.

Geosci. Model Dev. Discuss., https://doi.org/10.5194/gmd-2018-191
Manuscript under review for journal Geosci. Model Dev.
Discussion started: 23 August 2018

Geoscientific Model Development Discussions

Table 1. Comparison of pan-Arctic 3D sea-ice biogeochemical model configurations developed in various framework. dx: the horizontal resolution; dzo: the vertical resolution of the uppermost water column; dzi: the thickness of ice algal skeletal layer; i_0: the fraction of incoming shortwave radiation which penetrates through the snow surface; Shading: the attenuation of light by ice algae; and Runoff: the river discharge of nitrate.

Reference	Framework	dx	dzo	dzi	$i_{0,snow}$	Shading	Runoff
Dupont (2012)	MOM	$\sim$ 50 km	3.45 m	5 cm	0	no	yes
Jin et al. (2012)	POP	$\sim$ 40-50 km	10 m	3 cm	0	no*	no*
Watanabe et al. (2015)	COCO	$\sim$ 5 km	2 m	2 cm	1*	no	no*
Castellani et al. (2017)	MITgcm	$\sim$ 28 km	10 m	5 cm	0.3	yes	no
This study (EXP0)	NEMO	10-14.5 km	1 m	3 cm	0.15	yes	no

*Confirmed through personal communication with the lead author.

2.1 Ocean and sea ice physics (OPA-LIM2)

The physical ocean submodel is the Océan PArallélisé (OPA), which is a free-surface, hydrostatic, primitive-equation model developed for regional and global oean circulation studies (Madec, 2008). OPA is coupled to the submodel for sea-ice physics, namely the Louvain-la-Neuve sea Ice Model (LIM). The present study uses version 2 of LIM (LIM2; Fichefet and Maqueda, 1997; Bouillon et al., 2009) , consisting of a three-layer (one for snow and two for ice) dynamic-thermodynamic model.

To model ambient light available for ice algae and under-ice phytoplankton properly, we modified the module which computes the shortwave radiative transfer through snow and sea ice as shown schematically in Figure 1. In this module, the unreflected fraction (1-a) of the incoming shortwave radiation (F_{sw}) is parameterized as either being absorbed within a thin layer of surface snow and/or ice (defined as having thickness of 10 cm in NEMO v3.4) or penetrating through the snow and/or ice interior underneath this layer. This penetrating fraction is determined by a coefficient, i_0, which is set to zero for snow surface in the default configuration of LIM2 following Maykut and Untersteiner (1971). While this assumption of complete blockage of light may be a reasonable approximation for thermodynamic processes of snow and sea ice, this approximation is problematic for modelling sea-ice biogeochemistry. Specifically, the assumption implies that primary producers can not photosynthesize until snow disappears completely, which is inconsistent with the findings of many field observations that measure high algal biomass at the base of snow-covered sea ice (e.g. Leu et al., 2015). Furthermore, i_0 has been set to non-zero values in other sea-ice models in the case of thin or melting snow (Flato and Brown, 1996; Abraham et al., 2015). For these reasons, we use a non-zero value of i_0 and parameterize the light transmission through the snow column below the specified surface layer following the Beer-Lambert law. The value of i_0 was set to 0.15 following the 1D sea-ice biogeochemical modelling work of Vancoppenolle et al. (2010). The attenuation coefficient of snow was set to 10 m^{-1}, which falls within the observed range for melting and freezing snow (Grenfell and Maykut, 1977). The model sensitivity to i_0 is discussed in Section 4.2.

Geosci. Model Dev. Discuss., https://doi.org/10.5194/gmd-2018-191
Manuscript under review for journal Geosci. Model Dev.
Discussion started: 23 August 2018

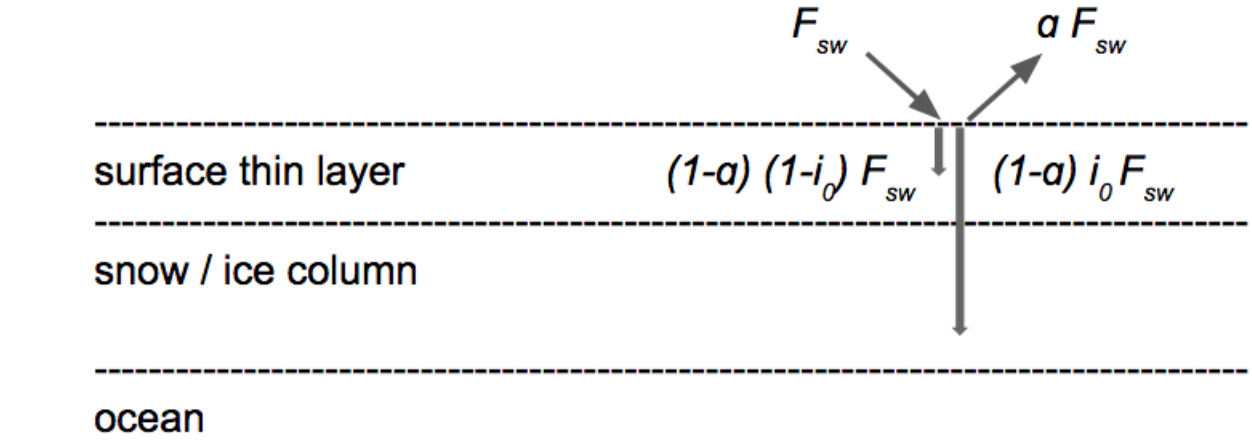

Figure 1. Shortwave radiative transfer through snow and sea ice modified from Figure 3.4 of Vancoppenolle et al. (2012). F_{sw} represents the incoming shortwave radiation, a fraction of which is reflected due to the surface albedo of snow or ice (a). The remaining fraction is either absorbed within the surface thin layer ($(1-a)(1-i_0)F_{sw}$) or penetrates into the snow and/or ice column below this layer ($(1-a)i_0F_{sw}$).

2.2 Ocean biogeochemistry (CanOE)

The submodel for ocean biogeochemistry adopted in the present study is the Canadian Ocean Ecosystem Model (CanOE), developed by the ocean modelling group at the Canadian Centre for Climate Modelling and Analysis (Christian et al, in prep.). This model has been developed for the latest version of the Canadian Earth System Model (Arora et al., 2011), which will be used in the next phase of the Coupled Model Intercomparison Project (CMIP6). CanOE simulates the lower trophic levels of marine ecosystems (nutrients, phytoplankton, zooplankton, and detritus) and biogeochemical cycling of key elements (carbon, oxygen, nitrogen, and iron). This model is built around the basic code structure of the Pelagic Interactions Scheme for Carbon and Ecosystem Studies (PISCES) version 2, the default submodel for ocean biogeochemistry of NEMO (Aumont et al., 2015). One advantage of CanOE over PISCES is that it is computationally more efficient as a result of having fewer state variables (19 vs 24) and fewer computationally expensive parameterizations (Christian et al, in prep.). In the present study, we made two modifications to CanOE. The first modification is the addition of an ocean sulfur-cycle model and the second modification is the parameterization of the photosynthetically active radiation (PAR).

2.2.1 Addition of an ocean sulfur cycle

Figure 2 shows a schematic of CanOE including the ocean sulfur cycle and the sea-ice biogeochemistry. The sulfur cycle model consists of two state variables: dissolved dimethylsulfoniopropionate (DMSPd) and dimethylsulfide (DMS). The ocean sulfur cycle is one-way coupled to CanOE as sulfur cycle processes depend on the state of the ecosystem, but not vice versa. The ocean sulfur-cycle model is based on Hayashida et al. (2017) with the following two modifications. First, the cellular DMSP content of modelled phytoplankton is derived from their carbon content as opposed to the chlorophyll content as in Hayashida

Geosci. Model Dev. Discuss., https://doi.org/10.5194/gmd-2018-191
Manuscript under review for journal Geosci. Model Dev.
Discussion started: 23 August 2018

Geoscientific Model Development Discussions

et al. (2017). This change was made because the intracellular DMSP-to-carbon (DMSP:C) ratio has been considered more thoroughly in observations than the DMSP-to-chlorophyll a ratio (e.g. Stefels et al., 2007). The DMSP:C ratios for small and large phytoplankton (respectively high and low DMSP producers) are set to 12 and 4 mmol:mol.

Also, the parameterization of sea-to-air flux of DMS was modified to account for the non-linear dependence of the flux on the open-water fraction (Loose et al., 2009):

$$F = f_{ow}^{0.4} k_{dms} DMS \tag{1}$$

where F is the DMS flux (μmol m^{-2} s^{-1}), f_{ow} is the open-water fraction (-), k_{dms} is the gas transfer velocity (m s^{-1}), and DMS (nM) is the DMS concentration in the uppermost layer of the water column.

2.2.2 Correction to the fractionation of under-ice PAR

The second modification to CanOE was made to the PAR fraction of incident solar radiation. PAR is the shortwave radiation in the 400-700 nm wavelength range, which is available for photosynthesis. In CanOE, PAR reaching the sea surface is 43% of the downwelling shortwave radiation, a well established estimate for PAR in open water (e.g. Morel, 1988). However, this assumption underestimates PAR reaching the sea surface under sea ice. The shortwave radiation penetrating through snow and ice is almost entirely PAR, as radiation outside of the 400-700 nm range is absorbed by the snow and ice (e.g. Zeebe et al., 1996). Thus, we have set the fraction of the downwelling shortwave radiation to unity when computing the sea-surface PAR under sea ice.

2.3 Sea-ice biogeochemistry

The submodel for sea-ice biogeochemistry is a modified version of a three-compartment (ice algae, nitrate, and ammonium) ecosystem based on Mortenson et al. (2017) and a two-compartment (DMS and DMSPd) sulfur cycle based on Hayashida et al. (2017).

Sea-ice biogeochemical processes are assumed to take place in a layer of fixed thickness at the ice base. The governing equation for any sea-ice biogeochemical state variable is:

$$\frac{\partial X}{\partial t} = -\nabla \cdot \left(\overrightarrow{U} X \right) + D \nabla^2 X + \mathrm{SMS}\left(X\right) \tag{2}$$

where X denotes the concentration of the state variable, $\overrightarrow{U}$ denotes the horizontal velocity field of sea ice, and D denotes the horizontal eddy diffusion coefficient. The first and second terms on the right hand side of Equation 2 represent horizontal transport by resolved (advection) and unresolved (eddy diffusion) motions, respectively. The third term represents biological and chemical sources and sinks of the state variable X. Note that while LIM2 computes the impact of mechanical redistribution (i.e. deformation due to ridging/rafting) on sea ice physical properties, these processes are neglected in computations of the sea ice biogeochemical state variable tendencies in the present study as the model uses a simple representation of the sea-ice biogeochemical layer as a layer of fixed thickness (3 cm) at the ice base.

Geosci. Model Dev. Discuss., https://doi.org/10.5194/gmd-2018-191
Manuscript under review for journal Geosci. Model Dev.
Discussion started: 23 August 2018

Geoscientific Model Development Discussions

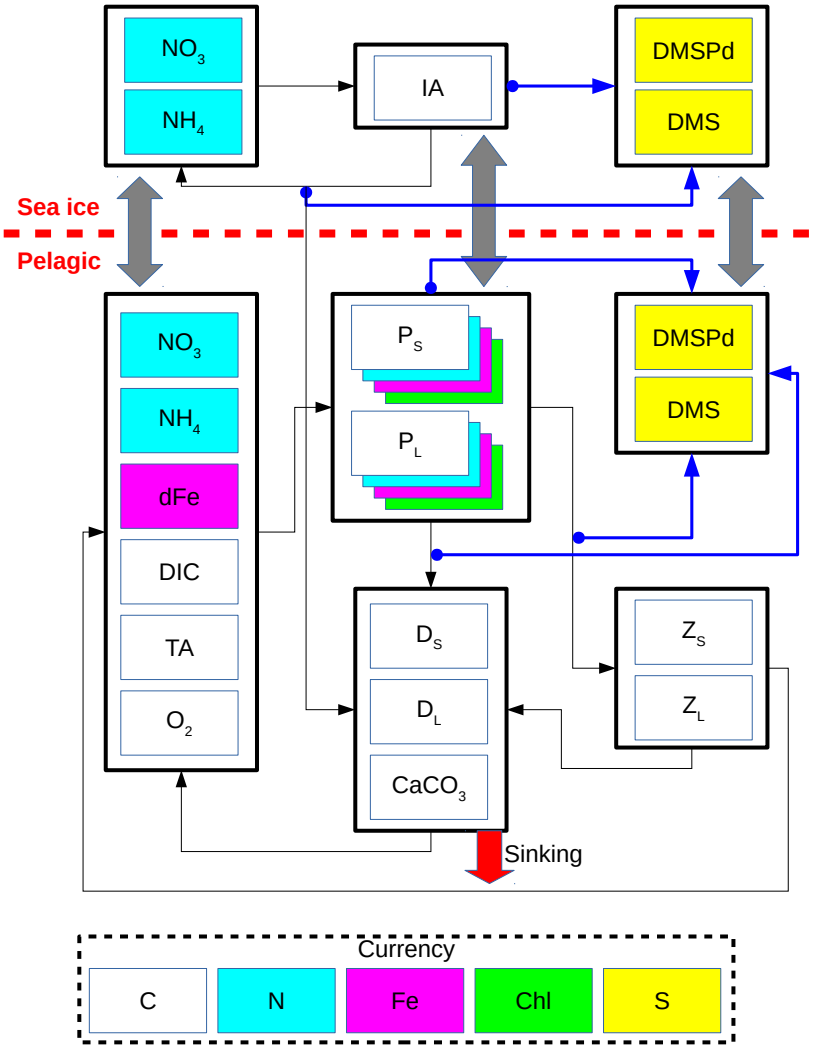

Figure 2. Schematic of the CanOE pelagic ecosystem model and associated sea-ice biogeochemistry and pelagic sulfur-cycle models. Black arrows indicate fluxes of carbon (C)/nitrogen (N)/iron (Fe) between compartments; blue arrows indicate sources of dissolved dimethylsulfoniopropionate (DMSPd); gray arrows indicate ice-ocean fluxes of nitrate (NO_3), ammonium (NH_4), ice algae (IA)/large phytoplankton (P_L), DMSPd, and dimethylsulfide (DMS). Flows of dissolved oxygen (O_2) are opposite to those of dissolved inorganic carbon (DIC) and are not explicitly illustrated. Detritus (D_S and D_L) and zooplankton (Z_S and Z_L) are denominated in C units but have implicit N and Fe pools according to fixed elemental ratios; phytoplankton (P_S and P_L) have separate state variables for each currency. O_2 and total alkalinity (TA) are their own currencies, but are shown as white here for simplicity; their sources and sinks follow well established stoichiometry relative to those of DIC. Sources and sinks of TA associated with the nitrogen cycle (Wolf-Gladrow et al., 2007) are included but not shown in the figure. The state variables dFe and $CaCO_3$ represent dissolved iron and calcium carbonate, respectively. The currencies Chl and S represent the chlorophyll a and sulfur, respectively.

Geosci. Model Dev. Discuss., https://doi.org/10.5194/gmd-2018-191
Manuscript under review for journal Geosci. Model Dev.
Discussion started: 23 August 2018

2.3.1 Advection and diffusion

Horizontal advection and eddy diffusion of sea-ice biogeochemical state variables are computed simultaneously and in the same way as the sea ice physical properties of LIM2 (i.e. snow and sea ice volume, heat content, and areal coverage). For advection, the scheme of Prather (1986) is applied. Eddy diffusion tendencies are computed explicitly and are set to zero at the ice edge. The horizontal diffusion coefficient (D) is set to 5 m^2 s^{-1}, as suggested byVancoppenolle et al. (2012). Readers are referred to Vancoppenolle et al. (2012) for further description of these processes. The impacts of advection and diffusion on modelled sea-ice biogeochemical state variables are discussed in Section 4.3.

2.3.2 New ice formation

In case of simulated horizontal accretion (i.e. an increase in sea ice concentration due to thermodynamic growth), the newly-formed ice is assumed to contain the same concentrations of sea-ice biogeochemical state variables as those in the underlying water column. Thus, the concentration of any sea-ice biogeochemical state variable is updated as follows:

$$X = \frac{SIC_{t-1}}{SIC_t} X^* + \frac{SIC_t - SIC_{t-1}}{SIC_t} X_{ui} \tag{3}$$

where SIC_{t-1} and SIC_t respectively denote the sea-ice concentrations in the previous and current time step. X^* denotes the concentration of the sea-ice biogeochemical state variables after the computation of advection and diffusion but prior to the computation of biological and chemical sources and sinks. X_{ui} denotes the concentration of the biogeochemical state variable in the uppermost layer of the water column under the ice. Equation 3 neglects the density difference between sea ice and seawater, and therefore violates mass conservation. However, this simplification has negligible effect on ocean biogeochemistry given the relatively-thin sea-ice biogeochemical layer as demonstrated in Hayashida et al. (2017). For ice algae only, a minimum biomass threshold is set at 10 mmol C m^{-3} in order to mimic reasonable overwintering biomass (Mortenson et al., 2017).

2.3.3 Biological and chemical sources and sinks

The biological and chemical processes represented as sources and sinks of the sea-ice biogeochemical state variables are described in detail in Mortenson et al. (2017) and Hayashida et al. (2017). For the ecosystem component, these processes include photosynthesis, mortality, and remineralization of dead organic matter. The growth rate of ice algae is dependent on ambient temperature, PAR, and nutrient concentrations (nitrate and ammonium). Note that the growth rate dependence on ice melt considered in Mortenson et al. (2017) has been neglected in the present study because: 1) our preliminary results indicated that ice algal blooms were generally insensitive to it; 2) the parameterization for ice melt limitation was applied for a specific location and might not be appropriate for other locations; and 3) the parameterization lacks observational evidence.

In addition to the computation of biological and chemical sources and sinks, processes relevant to the ice-ocean fluxes are computed, including molecular diffusive exchange of nutrients, release of all state variables into the water column due to basal ablation, and flushing of these variables through flows of water through the ice from rainfall and surface ablation.

Geosci. Model Dev. Discuss., https://doi.org/10.5194/gmd-2018-191
Manuscript under review for journal Geosci. Model Dev.
Discussion started: 23 August 2018

Table 2. List of model experiments

Name	Description	Duration
EXP0	Reference simulation.	1969-1979
EXP1	Same as EXP0 except that the atmospheric forcing was replaced by the CORE-II dataset.	1969-1979
EXP2	Same as EXP0 except that the snowfall and total precipitation for 1969-1978 were replaced by the original DFS dataset (i.e. daily-mean climatology).	1969-1979
EXP3	Same as year 1979 of EXP0 except that the light penetration through snow was impeded (i.e. i_0 was set to zero as in the original LIM2).	1979
EXP4	Same as year 1979 of EXP0 except that the advection and diffusion of sea-ice biogeochemical state variables were neglected (i.e. set to zero).	1979
EXP5	Same as year 1979 of EXP0 except that the shading effect of ice algae was neglected (i.e. set to zero).	1979

2.4 Experiments

In this study, we consider six model experiments (Table 2). The first experiment is a reference simulation (EXP0), designed to be the most realistic model solution which best agrees with observations. The 11-year duration of EXP0 is considered sufficient for the spin up of sea-ice and near-surface pelagic variables based on previous Arctic biogeochemical model studies (e.g. Dupont, 2012; Jin et al., 2012). The setup of EXP0 is described below. The rest of the experiments (EXP1-5) are designed to assess the sensitivity of the model simulations to changes in uncertain forcing data and parameter values.

2.4.1 Domain

The model domain is based on the North Atlantic and Arctic (NAA) configuration developed by the ocean modelling group at the University of Alberta (www.knossos.eas.ualberta.ca/xianmin/anha/model_configuration.html#naa). This configuration was built on the curvilinear orthogonal coordinate system of NEMO that has been successfully applied to study the freshwater budget of the Arctic Ocean in present (Hu and Myers, 2013) and future climates (Hu and Myers, 2014), as well as to investigate pelagic ecosystem processes in the Canada Basin (Steiner et al., 2015). The NAA domain includes the Arctic Ocean, the Canadian Arctic Archipelago, the northern Bering Sea, the northern North Atlantic Ocean, and the Nordic Seas (Figure 3). The horizontal resolution of the 568 $\times$ 400 grid varies from 10 km along the North American boundary to 14.5 km along the Eurasian boundary. Vertically, the ocean is divided into 46 layers with variable resolution, from approximately 1 m in the uppermost layer to 255 m in the bottommost layer. This vertical resolution is finer than that of the original NAA configuration in the upper layers (Figure 4). The bathymetry is based on the 1 arc-min global relief data (ETOPO1; Amante and Eakins, 2009) as described by Hu and Myers (2013). For numerical stability, each ocean grid cell is set to have at least 7 vertical levels, corresponding to a depth of approximately 20 m.

Geosci. Model Dev. Discuss., https://doi.org/10.5194/gmd-2018-191
Manuscript under review for journal Geosci. Model Dev.
Discussion started: 23 August 2018

Geoscientific Model Development Discussions
Open Access
EGU

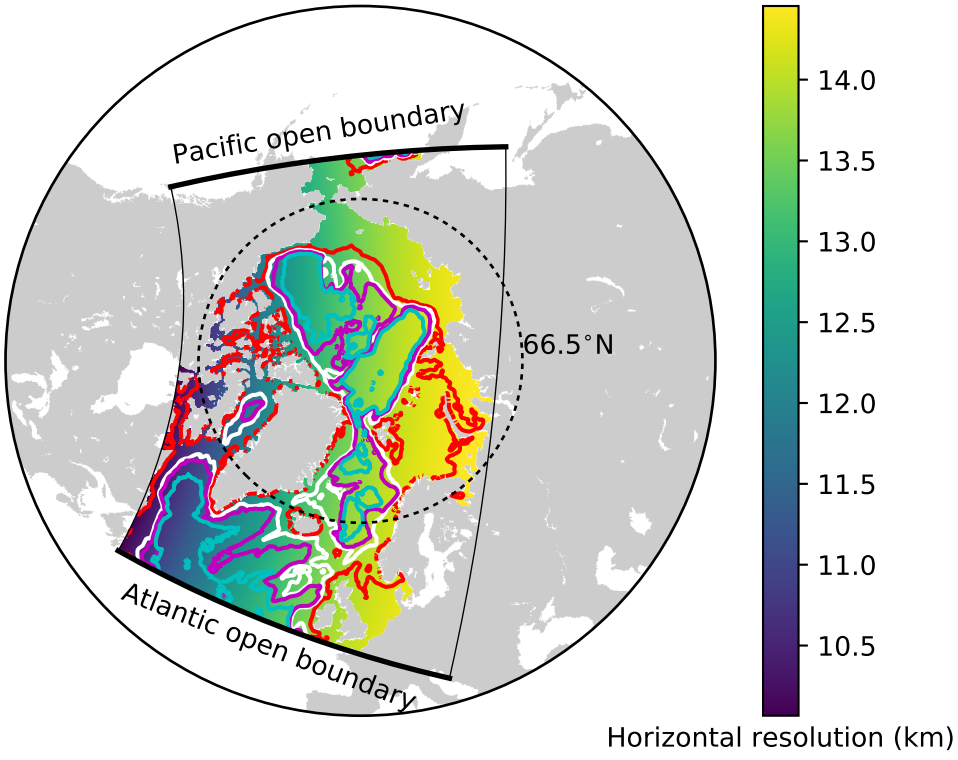

Figure 3. The domain of the North Atlantic and Arctic (NAA) configuration. The colour map represents the horizontal resolution and the contour lines denote the isobaths at 100 m (red), 1000 m (white), 2000 m (magenta), and 3000 m (cyan). The thick (thin) solid black lines indicate the locations of Atlantic and Pacific open (North American and Eurasian closed) boundaries.

2.4.2 Initial and lateral boundary conditions, runoff, and atmospheric forcing

The ocean was initialized from rest with temperature and salinity fields for January 1969 derived from the Ocean Reanalysis System 4 (ORAS4; Balmaseda et al., 2013). The initial snow depth, ice thickness, and ice concentration were respectively set to 0.1 m, 2.5 m, and 0.95 for grid cells with temperatures within 2 °C of the seawater freezing point. Elsewhere, these values were set to zero. The initial concentrations of nitrate, dissolved inorganic carbon, and total alkalinity were taken from the annual-mean fields of the GLobal Ocean Data Analysis Project version 2 (GLODAP2; Lauvset et al., 2016). The initial concentrations of dissolved oxygen were set to the annual-mean fields from the World Ocean Atlas 2013 Version 2 (WOA13; Garcia et al., 2014). The initial concentration of dissolved iron was set to 0.6 nM in the entire domain (Aumont et al., 2015). Because the model simulation starts at a time of low biological production (i.e. January 1), the remaining biogeochemical

Geosci. Model Dev. Discuss., https://doi.org/10.5194/gmd-2018-191
Manuscript under review for journal Geosci. Model Dev.
Discussion started: 23 August 2018

Geoscientific Model Development Discussions

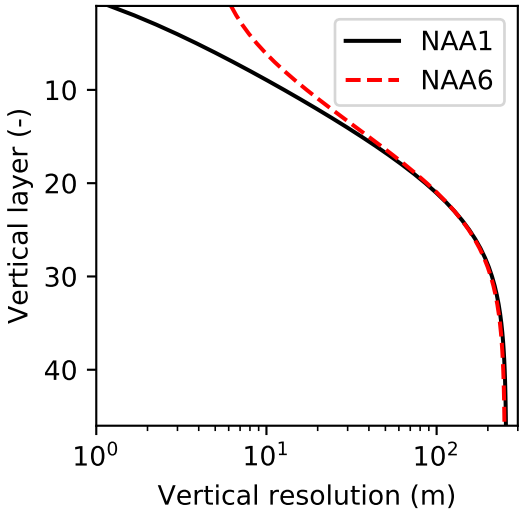

Figure 4. Comparison of the vertical resolution of the ocean model between the original NAA configuration (NAA6, i.e. approximately 6 m in the uppermost layer) and the configuration adopted in the present study (NAA1, i.e. approximately 1 m in the uppermost layer). Note the log scale on the x axis.

state variables in the ocean were initialized uniformly in space to arbitrarily low values. The initial concentrations of sea-ice biogeochemical state variables were set to the same values as their respective variables in the uppermost layer of the ocean.

Open boundary conditions were applied by a radiation-relaxation algorithm (Madec, 2008) along the Atlantic and Pacific boundaries of the model domain, while the other two boundaries (along North America and Eurasia) were assumed to be closed (Figure 3). The boundary temperature, salinity, and zonal and meridional current fields were interpolated from the interannual monthly-mean fields of ORAS4. The open boundary conditions for ocean biogeochemical state variables were the same as their initial conditions. The relaxation timescales were set to 1 day for inflow and 15 days for outflow. These values are identical to those used in Dupont et al. (2015), but differ from the original NAA configuration (Hu and Myers, 2013). Our preliminary experiments suggested that these changes were needed to prevent salinity drift. Because the feature to prescribe the open boundary conditions for the sea-ice prognostic variables was not available in NEMO version 3.4, these were set to zero for the sea-ice prognostic variables of LIM2 as well as the sea-ice biogeochemical state variables; this feature is available in the succeeding version of NEMO (version 3.6).

River discharge of freshwater was derived from the interannual monthly-mean product of Dai and Trenberth (2002). The river discharge of biogeochemical state variables was neglected, and therefore, was not addressed in this study. Additional external supplies of nutrients (i.e. dust deposition and sediment mobilization), which can be represented in CanOE, were neglected due to the lack of reliable data. Partial pressure of carbon dioxide in the atmosphere was derived from the monthly-mean Mauna Loa CO_2 data (www.esrl.noaa.gov/gmd/ccgg/trends/data.html).

Geosci. Model Dev. Discuss., https://doi.org/10.5194/gmd-2018-191
Manuscript under review for journal Geosci. Model Dev.
Discussion started: 23 August 2018

Geoscientific Model Development Discussions

Table 3. List of selected model parameters in the NEMO namelists

Name	Description	Unit	Value
	namelist		
rn_aht_0	Horizontal eddy diffusivity for oceanic active tracers	$m^{-2}\ s^{-1}$	5
	namelist_ice_lim2		
ahi0	Horizontal eddy diffusivity for sea-ice properties	$m^{-2}\ s^{-1}$	5
hiccrit	Thickness of newly-formed ice	m	0.6
pstar	Ice strength parameter	$N\ m^{-2}$	23,000
	namelist_top		
rn_ahtrc_0	Horizontal eddy diffusivity for passive tracers	$m^{-2}\ s^{-2}$	5
	namelist_pisces		
Tref	Reference temperature for photosynthesis, grazing, and remineralization	°C	10
chldeg	Chrolophyll oxidation rate	d^{-1}	0

The surface atmospheric conditions used to drive the sea-ice and ocean model simulations were derived from the Drakkar Forcing Set 5.2 (DFS; Dussin et al., 2016). The DFS dataset is high resolution in space (0.7°) and time (3-hourly for zonal and meridional wind speed at 10 m height and air temperature and specific humidity at 2 m height; and daily for incoming shortwave and longwave radiation, total precipitation, and snowfall) based on a combination of ERA-40 and ERA-interim reanalysis products (Uppala et al., 2005; Dee et al., 2011). The original DFS dataset (www.servdap.legi.grenoble-inp.fr/meom/DFS5.2/ALL) has missing data flags which cause a simulation crash in some years. As a substitute, we used a modified version provided by Clark Pennelly at the University of Alberta (personal communication). Furthermore, in EXP0, the DFS snowfall and the total precipitation for year 1979 were used repeatedly for the simulation over the period 1969-1978, as opposed to the 1979-2012 daily climatology (due to the lack of adequate observations to construct the dataset for those years individually; Dussin et al., 2016). This modification was necessary to simulate adequate snow depths (discussed further in Section 4.1).

2.4.3 Additional settings

The time step of the model integration was 20 minutes. Unlike Hu and Myers (2013), no additional treatments for modelled temperature, salinity and wind-stress fields near the open boundaries were necessary since no obvious drift was apparent in the simulated fields. Table 3 displays some of the model parameters that were modified from their default values in NEMOv3.4. For a complete list of the parameters, readers are referred to the source-code repository (www.gitlab.com/hakasehayashida/canoe-dms/tree/version1/CONFIG/cmoc08_naa1/EXP00). The coefficients for horizontal eddy diffusion for oceanic and sea-ice tracers (rn_aht_0, ahi0, and rn_ahtrc_0) were reduced to keep diffusion relatively small compared to resolved dynamical processes, as recommended by Vancoppenolle et al. (2012). The other two parameters (hiccrit and pstar) were adjusted to improve the modelled sea ice volume and extent. Lastly, two parameters of CanOE (Tref and chldeg) were adjusted to simulate reasonable annual primary production in the Arctic Ocean.

Geosci. Model Dev. Discuss., https://doi.org/10.5194/gmd-2018-191
Manuscript under review for journal Geosci. Model Dev.
Discussion started: 23 August 2018

2.4.4 Output

The output of the model experiments was saved as annual means for the first ten years (1969-1978) and five-day means for the final year (1979). Ice (snow) volume was defined as the sum of the product of grid-cell-mean ice thickness (snow depth) and the grid-cell area. Ice extent was defined as the areal sum of all grid cells with an ice concentration of at least 0.15. Primary productivity within sea ice was quantified in terms of depth-integrated (bottom 3 cm) gross primary productivity (GPP), whereas primary productivity within water column was expressed in terms of depth-integrated (upper 90 m) net primary productivity (NPP). GPP was used for ice algae because the linear loss term for ice algae in our model accounts for processes other than just respiration, and therefore NPP cannot be derived simply by subtracting the linear loss term from the photosynthetic growth (i.e. GPP). In any case, the difference between NPP and GPP may be small for ice algae, as a previous incubation experiment suggests that NPP accounts for 60 to 100 % of GPP in the bottom layer of Arctic sea ice (Table 4 of Gosselin et al., 1997). Any grid cell whose ice concentration is 0.15 or greater was considered "under-ice" following Zhang et al. (2010). To investigate the interannual variability in pan-Arctic primary productivity, the ice algal GPP, phytoplankton NPP, and under-ice NPP were integrated annually and horizontally to derive respective pan-Arctic annual quantities. The term pan-Arctic is defined here as the region north of the Arctic Circle (66.5 °N). The pan-Arctic mean refers to an area-weighted average over the region north of the Arctic Circle. This areal restriction allows consistent comparison to some previous studies (e.g. Legendre et al., 1992; Jin et al., 2012).

2.4.5 PIOMAS and SIIV3 data products

The modelled sea-ice properties were evaluated against the following observationally-based data products: the the Pan-Arctic Ice Ocean Modeling and Assimilation System (PIOMAS) and Sea Ice Index Version 3 (SIIV3) data products. Although these products are considered here as the best data products presently available, note that these products have their own biases that could result in mismatches with our model results.

PIOMAS is a regional coupled sea ice-ocean circulation model that also assimilates some observational data (Zhang and Rothrock, 2003; Schweiger et al., 2011). The daily-mean time series of PIOMAS ice volume were obtained from www.psc.apl.uw.edu/research/projects/arctic-sea-ice-volume-anomaly/data. The monthly-mean ice thickness and ice concentration gridded data products of PIOMAS were also used for spatial comparison (Dirkson et al., 2016).

SIIV3 provides an estimate for ice extent based on sea-ice concentration fields derived from passive microwave radiometers (Windnagel et al., 2017). The daily-mean SIIV3 ice extent time series were obtained from the National Snow and Ice Data Center website (www.nsidc.org/data/G02135/versions/3). For the year 1979, this data product is available for 182 days (i.e. every other day on average), which is sufficient to compare with the 5-day-mean model output.

Geosci. Model Dev. Discuss., https://doi.org/10.5194/gmd-2018-191
Manuscript under review for journal Geosci. Model Dev.
Discussion started: 23 August 2018

3 Reference simulation (EXP0)

3.1 Interannual variability during spin up

The annual-mean time series of modelled snow and ice volumes, ice extent, seawater nitrate, and ice algal and phytoplankton biomass over the 11 years of EXP0 are shown in Figure 5. This time period can be considered as sufficiently long to spin up some of these quantities, while others may require additional years to spin up. However, none of these quantities reach a steady state in the current setup as the model was driven by interannual surface and lateral boundary conditions. The aim of the present analysis is to diagnose potential drifts by examining the character of temporal variability starting from the initial year. In summary, no substantial drifts are simulated in any of the quantities considered.

The annual-mean modelled snow volume stabilized around 0.8×10^3 km^3 after an initial drop of about 0.1×10^3 km^3 from year 1969 to 1970 (Figure 5a), indicating a spin-up period of a year or so. In contrast, the annual-mean modelled ice volume variations showed an initial reduction during 1969-1971 followed by an overall increase during 1973-1979. The relatively short duration of this simulation does not allow us to distinguish between trends and slow interannual variability, so we cannot determine if the ice volume has spun up based solely on this analysis; this is addressed in a follow up study. A previous pan-Arctic regional model study of Watanabe (2013) showed a spin-up period of 10 years for modelled ice volume based on a simulation using a fixed annual cycle atmospheric forcing and restoring of temperature and salinity.

Modelled ice extent showed a decrease in the first 6 years followed by a stabilization in the last 5 years, suggesting that this quantity spun up at year 1975 (Figure5b). This spin-up time is similar to that found in the pan-Arctic model study of Jin et al. (2012), in which their modelled ice area and extent became comparable to the observations after the first 6 years of simulation.

The annual-mean modelled seawater nitrate concentration integrated over the upper 90 m of the water column in the entire model domain showed both increases and decreases during the 11 years (Figure5b), although the size of the fluctuation ($\sim$20 mmol N m^{-2}) is small relative to its mean state ($\sim$490 mmol N m^{-2}). Similarly to ice volume, a longer simulation would be needed to distinguish between trends and interannual variability in the modelled nitrate concentration. A previous pan-Arctic model study of Dupont (2012) indicated a spin-up period of at least a decade for nitrate in the upper 100 m water column for the model domain he considered. The modelled primary producers (ice algae and phytoplankton) appear to have spun up within a year of the model simulation, as their annual primary production fluctuates around a steady mean following the first year (Figure 5c).

3.2 Comparison of sea-ice physical properties with PIOMAS and SIIV3 during the year 1979

3.2.1 Seasonal variability

To assess the performance of the model simulation of sea ice, the seasonal variability of modelled ice volume and extent in EXP0 were compared to PIOMAS and SIIV3 (Figure6a and b) for the year 1979. This year corresponds to the first full year available for these data products. The ice volume in both EXP0 and PIOMAS was at its annual maximum in late April (April 25 vs 28) and at its annual minimum in September (September 10 vs 21). The ice extent in EXP0 and SIVV3 was

Geosci. Model Dev. Discuss., https://doi.org/10.5194/gmd-2018-191
Manuscript under review for journal Geosci. Model Dev.
Discussion started: 23 August 2018

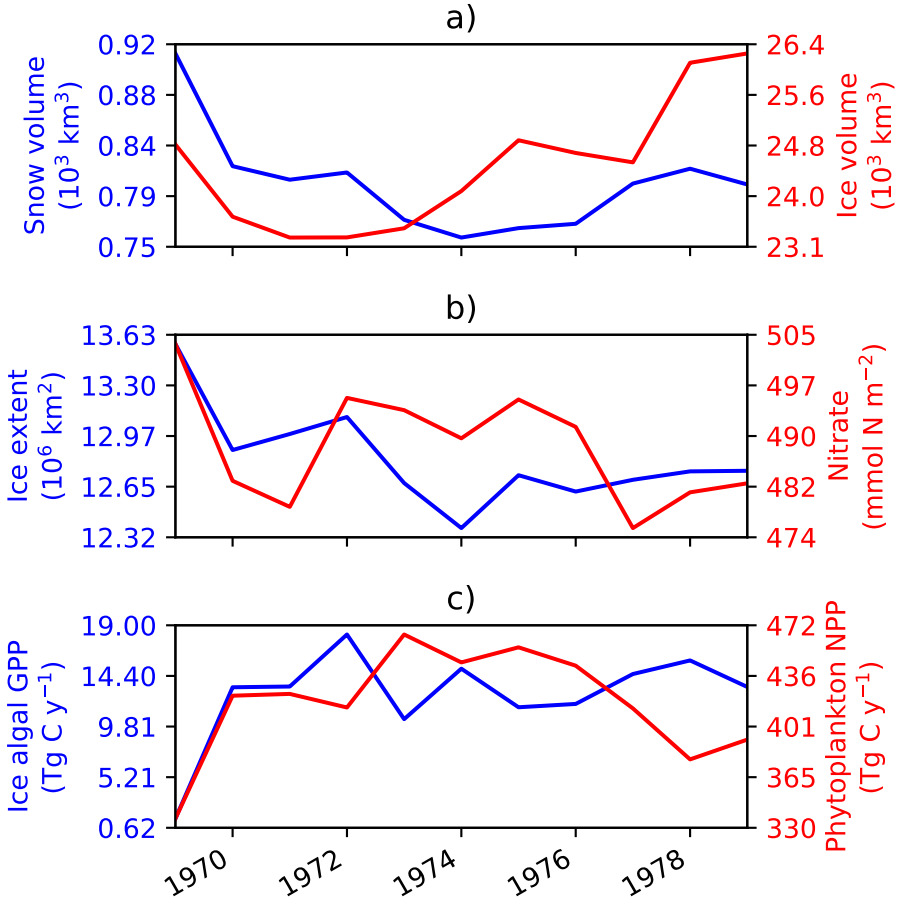

Figure 5. Time series of annual-mean modelled a) snow and ice volumes, b) ice extent and depth-integrated (90 m) seawater nitrate concentration, and c) depth-integrated (3 cm) ice algal GPP and depth-integrated (90 m) phytoplankton NPP in EXP0. The depth-integrated quantities represent averages over the entire model domain.

Geosci. Model Dev. Discuss., https://doi.org/10.5194/gmd-2018-191
Manuscript under review for journal Geosci. Model Dev.
Discussion started: 23 August 2018

at its annual maximum in March (March 24 vs 1) and at its annual minimum in September (September 25 vs 21). Given the difference in the frequency of the model output and these data products (5-day vs daily), the timings of the ice volume maximum and the ice extent minimum are comparable. The most prominent disagreement is in the timing of the ice extent maximum in which EXP0 lags by a few weeks. The seasonal recession of Arctic sea ice started later in EXP0 partly because our domain excludes lower-latitude regions that were ice-covered in 1979 (e.g. the Sea of Okhotsk and the Gulf of Saint Lawrence), and the seasonal retreat of sea ice in these areas occurred earlier (confirmed using the Sea Ice Spatial Comparison Tool: www.nsidc.org/arcticseaicenews/sea-ice-comparison-tool).

The ice volume is slightly higher in EXP0 than PIOMAS throughout the year, with the largest difference of about 3000 km^3 taking place in May-June. The ice extent, on the other hand, is generally lower in EXP0 than SIIV3, and their difference is greater than 1×10^6 km^2 during the season of greatest extent (December-May). Much of this difference can be attributed to the fact that the model domain excludes regions that are usually ice covered during that period, such as Hudson Bay (covering a surface area of 1.23×10^6 km^2) and the Sea of Okhotsk (1.58×10^6 km^2). During the remainder of the year, the modelled ice extent is in closer agreement with SIIV3 (especially in August-September).

3.2.2 Spatial variability

Figure 7 shows the spatial variability in modelled March- and September-mean ice thickness fields in EXP0 and PIOMAS. The extent of modelled Arctic sea ice can be inferred from the locations of ice edge, defined here as the contour of ice concentration of 0.15 (Figure 7a,b,d,e). Overall, the locations of the ice edge within our model domain are similar between EXP0 and PIOMAS for both March and September. Beyond the model domain, the ice coverage in March extends to Hudson Bay and the Sea of Okhotsk in PIOMAS (Figure7b). The March-mean ice thickness distribution in EXP0 consists of: a zonal band of >5-m-thick ice along the coast between north of Greenland and north of the western edge of the Canadian Arcitc Archipelago; and a region of relatively thick ice (∼4 m) in the Arctic Basin north of the East Siberian Sea (Figure7a). The zonal band is also present in PIOMAS, although it is restricted to the north of Greenland (Figure7b). The thick ice region in the Arctic Basin north of the East Siberian Sea, on the other hand, is absent in PIOMAS. Besides these regions entailing the zonal band and the blob, EXP0 generally simulated thicker ice than PIOMAS in the Greenland Sea and various shelf regions (Figure7c). On the other hand, EXP0 simulated thinner ice than PIOMAS in the Canadian Polar Shelf, the Chukchi Sea, the Barents Sea, the Kara Sea, and an area near the North Pole (Figure7c).

In September, the most notable features in the ice thickness distribution are the presence of: thin (<2 m) ice (relative to the surroundings) in an area near the North Pole in EXP0 (Figure 7d); and thick (>5 m) along the coast of Siberia in PIOMAS (Figure 7e). The latter feature seems unrealistic considering that: it is thicker in September than in March; and it is thicker than the multi-year ice present along the band north of the Canadian Arctic Archipelago and Greenland. Both of these features result in negative values in the ice thickness difference between the model and PIOMAS (Figure 7f). Besides these regions, the difference is also negative and high (∼3 m) in the Canadian Polar Shelf; this could be due to the fact that the horizontal resolution of PIOMAS (∼22 km; Zhang et al. (2010)) may be too coarse to resolve the circulation through these relatively narrow channels, resulting in the simulation of too thick first-year ice in this region at this particular time of the year. The

Geosci. Model Dev. Discuss., https://doi.org/10.5194/gmd-2018-191
Manuscript under review for journal Geosci. Model Dev.
Discussion started: 23 August 2018

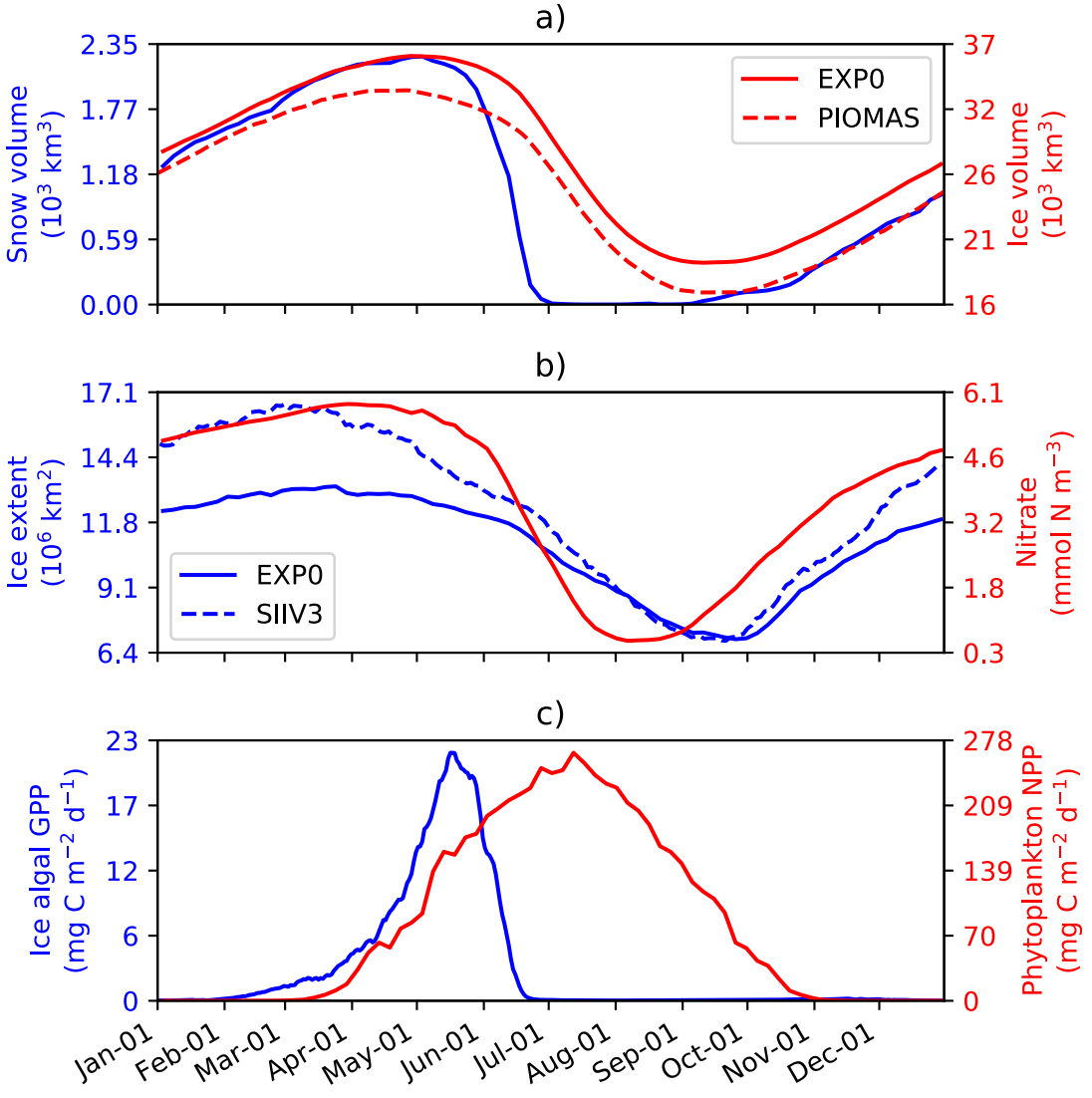

Figure 6. Time series of 5-day-mean modelled a) snow and ice volumes, b) ice extent and pan-Arctic-mean surface seawater nitrate concentration, and c) pan-Arctic ice algal and phytoplaknton daily NPP during 1979 in EXP0. The dashed lines in a) and b) represent the daily-mean ice volume and extent of PIOMAS and SIIV3, respectively.

Geosci. Model Dev. Discuss., https://doi.org/10.5194/gmd-2018-191
Manuscript under review for journal Geosci. Model Dev.
Discussion started: 23 August 2018

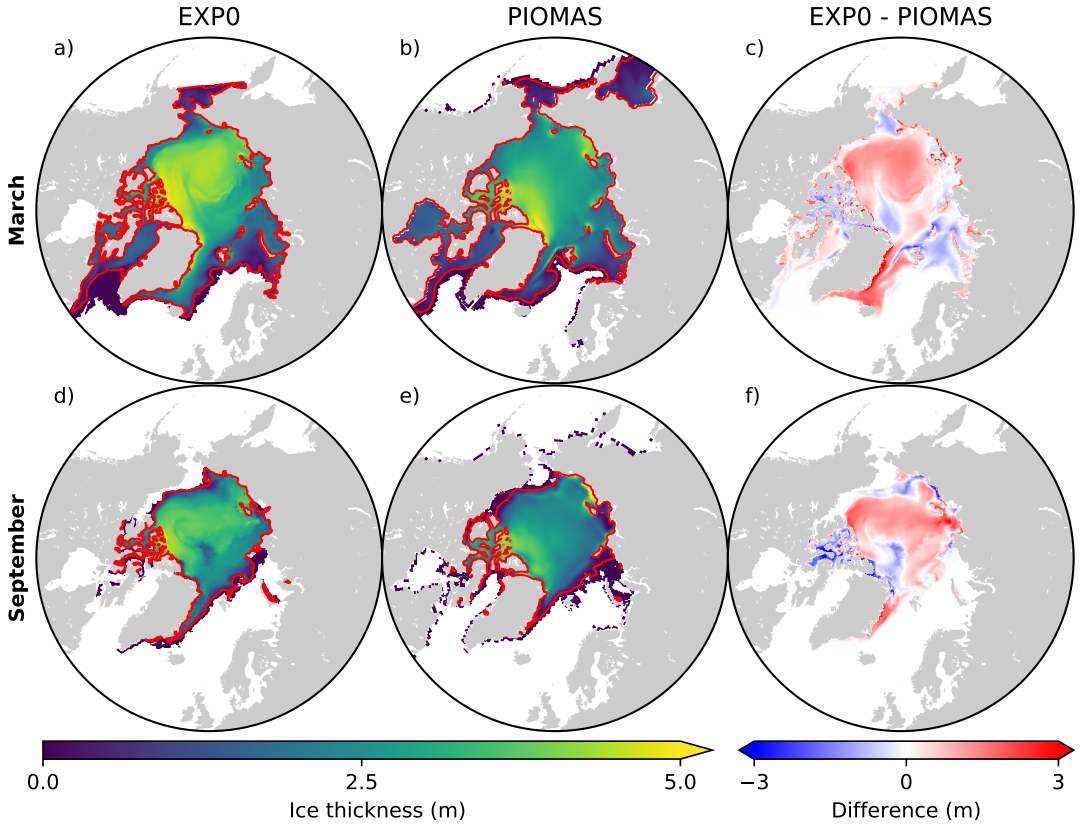

Figure 7. Spatial distributions of monthly-mean ice thickness in EXP0 (a,d) and the PIOMAS product (b,e) and their difference (c,f) for March and September in 1979. In a), b), d), and e), the red lines represent the ice edge defined here as the contour of ice concentration of 0.15. In c) and f), the comparison is restricted to the NAA domain because the ice thickness fields of PIOMAS were interpolated onto the NAA grid in order to perform a grid-to-grid comparison.

ice thickness difference is positive in the Arctic Basin, part of the East Siberian Sea, and the Laptev Sea as well as along the eastern coast of Greenland.

3.3 Primary productivity of ice algae and phytoplankton

3.3.1 Seasonal variability

Figure 6 shows the seasonal variability in modelled pan-Arctic-mean ice algal GPP and phytoplankton NPP during 1979 (panel c) along with relevant environmental factors (panels a and b). The ice algal GPP started increasing in early February, peaked in mid May, sharply declined in late May-early June, and was near zero by late June. The start of the decline of the ice algal GPP

Geosci. Model Dev. Discuss., https://doi.org/10.5194/gmd-2018-191
Manuscript under review for journal Geosci. Model Dev.
Discussion started: 23 August 2018

Geoscientific Model Development Discussions

coincided with the decline of the ice volume (Figure 6a) demonstrating that the decline was driven by the release of ice algae as a result of ice melt. The seasonal progression of the ice algal production is similar to Jin et al. (2012). The phytoplankton NPP started increasing in early March, peaked in early July, and decreased to near zero by the end of October (Figure 6d). At the peak in phytoplankton NPP, the pan-Arctic-mean surface seawater nitrate concentration was below 1 mmol N m^{-3} and remained so until the end of August (Figure 6b).

3.3.2 Spatial variability

Figure 8 shows the spatial distribution of annual-mean snow depth and surface seawater nitrate, and ice algal annual GPP and phytoplankton annual NPP for 1979. The largest values of ice algal annual GPP (>10 g C m^{-2} y^{-1}) are present in the coastal regions of Baffin Bay, the Canadian Polar Shelf, the Chukchi Sea, the East Siberian Sea, and the Kara Sea (Figure 8c). All of these regions have relatively thin snow (less than 0.1 m; Figure 8a), demonstrating the control of light on ice algal growth. In contrast, the nutrient control on ice algal production is less pronounced; although high ice algal GPP usually concides with high surface seawater nitrate, it is also present in a few areas where the nitrate levels are relatively low (Baffin Bay and Chukchi Sea; Figure 8b). Overall, ice algal production is mostly confined to shelf regions (water depth <100 m; Figure 3), consistent with previous model studies (Deal et al., 2011; Dupont, 2012; Jin et al., 2012, 2018). However, the values reported in Deal et al. (2011), Jin et al. (2012), and Jin et al. (2018) are representative of NPP, while those of Dupont (2012) and the present study represent GPP; comparisons should be made with this difference in mind.

There are a few noteworthy similarities and differences in the spatial variability in modelled ice algal annual production between the present study and previous model studies. All studies show a moderate-to-high level of ice algal production in Baffin Bay. In contrast, disagreement in the ice algal production is found along the eastern coast of Greenland and in the Bering Sea; the values along the eastern coast of Greenland are moderate (5-10 g C m^{-2} y^{-1}) in Deal et al. (2011) and Jin et al. (2012), while they are low (less than 5 $^{-2}$ y^{-1}) in Dupont (2012), Jin et al. (2018), and the present study. Similarly, although Bering Sea is identified as a region of high ice algal production by Deal et al. (2011), Jin et al. (2012), and Jin et al. (2018), Dupont (2012) and the present study simulate low ice algal production in this region. A possible explanation for the lower ice algal production in this region in the latter studies is due to an insufficient nutrient supply from the Pacific boundary as discussed in Dupont (2012). Lastly, the recent study by Jin et al. (2018) finds the Sea of Okhotsk to be a region of elevated ice algal annual production, which we are unable to assess in the present study due to the limited model domain.

The modelled phytoplankton annual NPP is high (>100 g C m^{-2} y^{-1}) in the Atlantic and the Pacific sectors with little to no ice cover, moderate (50-100 g C m^{-2} y^{-1}) in the shelf seas along the North American and the Eurasian continents, and low (<50 g C m^{-2} y^{-1}) in the interior of the Arctic Ocean (Figure8d). These findings are in both qualitative and quantitative agreement with the results of five different models and satellite-based estimates (Figure 1 of Popova et al., 2012).

3.3.3 Interannual variability

The modelled pan-Arctic ice algal annual GPP in EXP0 ranged from 10.5 to 18.2 Tg C y^{-1} for the period 1970-1979, excluding the initial spin-up year. While this value is on the lower end of the range of observation-based NPP estimates (9-73 Tg C y^{-1};

Geosci. Model Dev. Discuss., https://doi.org/10.5194/gmd-2018-191
Manuscript under review for journal Geosci. Model Dev.
Discussion started: 23 August 2018

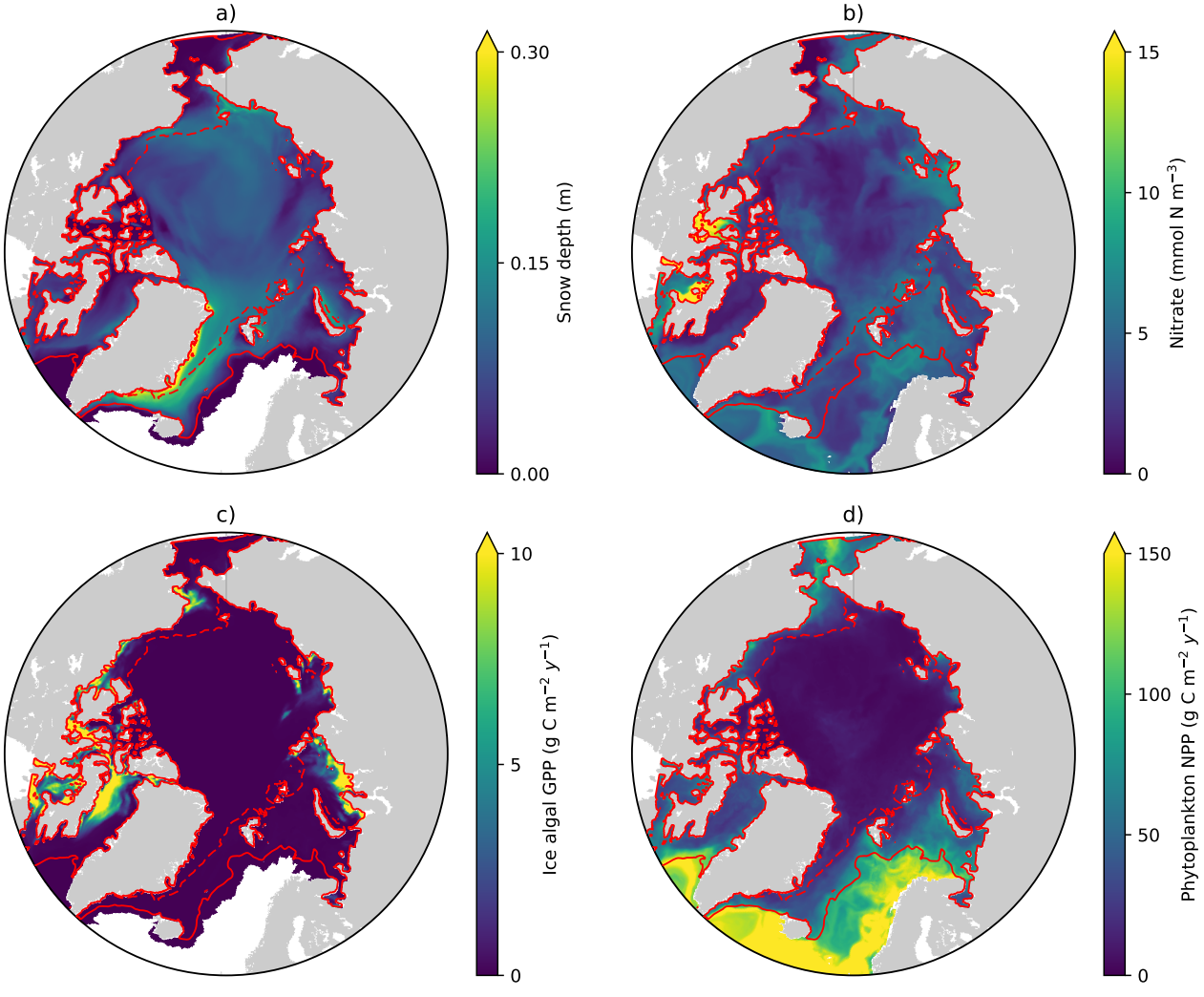

Figure 8. Spatial distribution of annual-mean a) snow depth and b) surface seawater nitrate concentration, and c) depth-integrated (bottom 3 cm) ice algal annual GPP and d) depth-integrated (upper 90 m) phytoplankton annual NPP in 1979 in EXP0. The solid and dashed red lines represent the contour of monthly-mean ice concentration of 0.15 in March and September, respectively.

Legendre et al., 1992), the upper bound (73 Tg C y^{-1}) accounts for contribution from mat and strand communities that are not represented in our model. Furthermore, this value is close to the decadal mean of the annual NPP (10.1 Tg C y^{-1} for 1998-2007) simulated by Jin et al. (2012). Direct comparisons with the results of Deal et al. (2011) and Dupont (2012) are not possible because the reported values in those studies include contributions from below the Arctic Circle. The modelled pan-Arctic phytoplankton annual NPP in EXP0 ranged from 378 to 465 Tg C y^{-1}, which is in line with the observation-based estimate (>329 Tg C y^{-1}; Total High Arctic) of Sakshaug (2004), the satellite-based estimate (419 Tg C y^{-1} for 1998-2006) of Pabi et al. (2008), and the model-based estimate (627 Tg C y^{-1} for 1998-2006) of Jin et al. (2012).

3.4 Vertical distribution of salinity, nitrate, chlorophyll a, and DMS in the upper water column

The seasonal variability of pan-Arctic-mean seawater salinity, nitrate, chlorophyll a, and DMS in the upper 15 m of the water column is shown in Figure 9. During the summer, a prominent freshening of the uppermost layer occurs as a result of ice melt (Figure 9a). This freshening results in formation of a thin layer of low-salinity water known as meltwater lens, which strengthened the stratification and reduced the mixing with the underlying water column. The formation of the lens coincided with the bloom of modelled phytoplankton, resulting in the depletion of nitrate first in the uppermost model layer and then in the underlying layers (Figure 9b). Nutrient depletion in the near surface then results in formation of subsurface chlorophyll a and DMS maxima during the latter half of July (Figure 9c and d).

These ice-associated physical and biogeochemical processes took place within a relatively shallow upper water column (∼10 m), and would have been impossible to simulate with a model of coarse vertical resolution. It is for this reason that the near-surface vertical resolution of the NAA configuration considered in the present study is finer than that of the original configuration (6 m in the uppermost layer; Hu and Myers, 2013). Although modelling these small-scale processes probably has negligible effect on bulk quantities such as depth-integrated NPP, it can have an impact on processes happening right at the air-sea or ice-sea interface (e.g. gas fluxes). To illustrate this point, the time series of modelled pan-Arctic-mean seawater DMS concentration in the uppermost layer of the water column (about 1 m) was compared with the concentration averaged over the top four layers (about 12 m) as a proxy for values simulated by a coarse-vertical-resolution model (Figure 10).

DMS concentration is higher in the uppermost layer than in the 12-m layer throughout most of April-September, but slightly smaller in August (Figure 10b). The concentration difference is largest (up to about 20 %) in June-July. The largest DMS concentrations are found in the upper 1 m until the formation of the subsurface maximum (Figure 9c). Overall, the annual-mean DMS concentration averaged over the upper 12 m of the water column is 9 % lower than in the upper 1 m. Considering that this difference is present primarily during the ice melt period, and therefore that the sea-surface DMS is capable of being released into the atmosphere, the sea-to-air DMS flux would be underestimated by a similar amount using the 12-m resolution time series.

Geosci. Model Dev. Discuss., https://doi.org/10.5194/gmd-2018-191
Manuscript under review for journal Geosci. Model Dev.
Discussion started: 23 August 2018

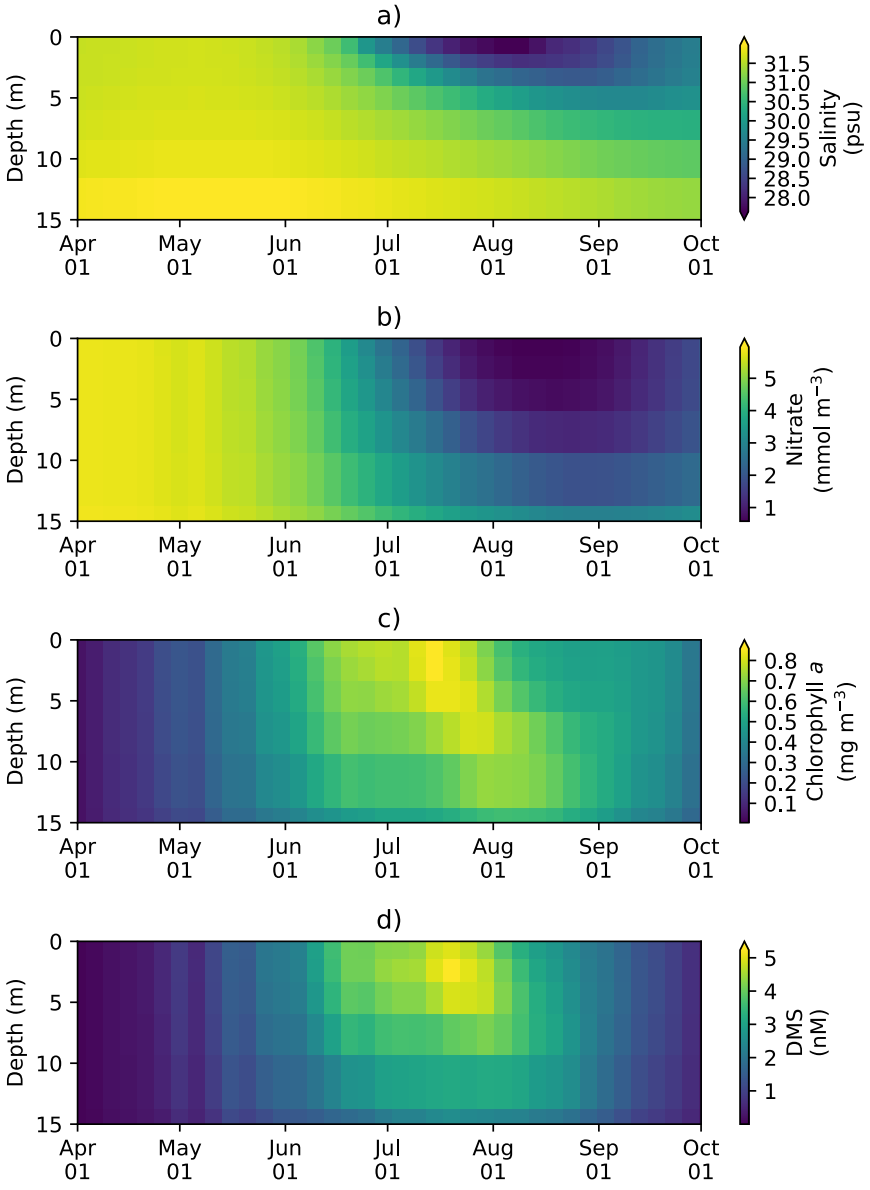

Figure 9. Time series of 5-day- and pan-Arctic-mean seawater a) salinity, b) nitrate, c) chlorophyll a, and d) DMS in the upper 15 m of the water column during April-September in 1979 of EXP0.

Geosci. Model Dev. Discuss., https://doi.org/10.5194/gmd-2018-191
Manuscript under review for journal Geosci. Model Dev.
Discussion started: 23 August 2018

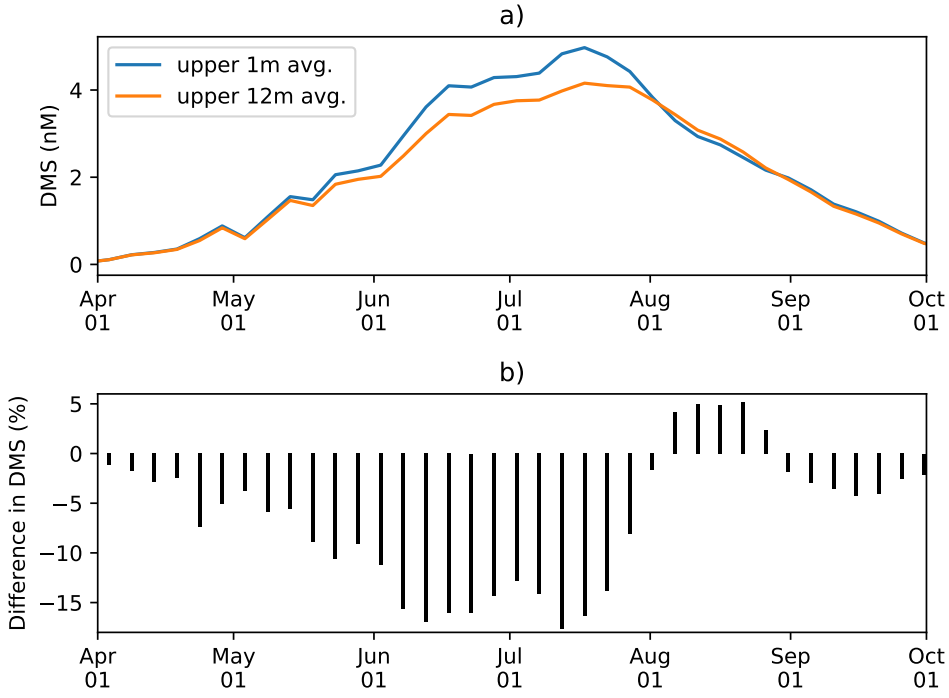

Figure 10. a) Time series of 5-day- and pan-Arctic-mean seawater DMS a) in the uppermost layer (∼1 m; blue) and averaged over the upper four layers (∼12 m; orange) during April-September in 1979 of EXP0. b) The percentage difference between the two time series (the 1-m average minus the 12-m average, divided by the 1-m average).

4 Sensitivity experiments (EXP1-5)

4.1 Snowfall forcing frequency (EXP1 and 2)

Two sensitivity experiments (EXP1 and EXP2) were performed with the identical setup as EXP0 except for a change to the atmospheric forcing. In EXP1, all the forcing fields were replaced by the CORE-II dataset used in the original NAA configuration (Hu and Myers, 2013). In EXP2, the snowfall and total precipitation fields over the period 1969-1978 were replaced by their respective 1979-2012 daily climatological values as in the original DFS dataset (Dussin et al., 2016).

A comparison of the pan-Arctic-mean snowfall rates between the CORE-II and DFS datasets illustrates the differences between these datasets (Figure 11a). The monthly CORE-II dataset varies from approximately 1 to 2.4 mm d^{-1}, while the range of the DFS dataset is three times as large (from nearly 0 to about 4.4 mm d^{-1} for the year 1979) most likely due to the difference in the temporal resolution of the datasets. The lack of high frequency variability in the DFS daily climatology is evident from the comparison of the DFS dataset between 1969-1978 and 1979. The daily climatology ranges approximately from 0.2 to 2.2 mm d^{-1}, less than a half of the range for the individual daily averages for 1979. The annual-mean CORE-II

Geosci. Model Dev. Discuss., https://doi.org/10.5194/gmd-2018-191
Manuscript under review for journal Geosci. Model Dev.
Discussion started: 23 August 2018

snowfall rate is higher than that of the DFS dataset in all of these years. Between the annual mean of the DFS daily climatology and that of the individual daily averages for 1979, the former is slightly higher.

Figure 11b shows a comparison of the modelled pan-Arctic annual-mean snow depth among EXP0, EXP1, and EXP2. The snow depth was substantially lower in EXP1 and EXP2 than in EXP0 throughout the period 1969-1979, except for 1969 (in which year the snow depth is affected by its initial value). In EXP2, the extremely-low snow depth somewhat recovered in 1979.

Figure 11c-e shows a spatial comparison of the modelled annual-mean snow depth over the period 1970-1978 (excluding the first and the last year of simulations). There is a clear difference in the distribution between EXP0 and the other two experiments; the ice pack was generally covered by moderate amount of snow ($\sim$0.1 m) in EXP0, while in EXP1 and EXP2, most regions were nearly snow-free. These results of the latter two experiments are inconsistent with the available snow depth climatology indicating the presence of considerably thicker (>0.2 m) annual-mean snow cover over the Arctic Basin (Warren et al., 1999). As a result of these biases, the modified DFS dataset was used as the reference simulation, rather than the CORE-II dataset or the original DFS dataset.

It is interesting that the modelled pan-Arctic annual-mean snow depth was higher in EXP0 than EXP1 even though the prescribed annual-mean snowfall rate was consistently higher in the latter experiment (Figure 11a). Furthermore, the recovery of the modelled snow depth in 1979 of EXP2 is also interesting given that there is essentially no change in the total snowfall amounts between 1978 and 1979. These results indicate a high sensitivity of the modelled snow depth to the frequency range contained in the snowfall dataset. This interpretation is reinforced by the fact that the modelled snow depth is also sensitive to the parameter nn_fsbc, which defines the frequency of the computation of surface boundary conditions and sea-ice physics relative to that of ocean dynamics. Figure 12 compares the annual-mean modelled snow depths for year 1970 of EXP2 with those of the simulations that varied nn_fsbc from the default value of 1 (i.e. the time step for surface boundary condition and sea-ice physics is identical to the ocean time step) to 5 and 10 (i.e. surface boundary condition and sea-ice physics are computed at every 5 and 10 ocean time steps, respectively). We found that setting nn_fsbc to 5 and 10 both increased the pan-Arctic-mean modelled snow depth although regional differences exist (Figure 12). This sensitivity to the frequency content of the input snowfall dataset and the frequency of coupling to the ocean is a model artifact. A more detailed analysis of this artifact (and its elimination) is outside of the scope of this study.

4.2 Light penetration through snow column (EXP3)

Figure 13 compares the modelled sea-ice physical and biogeochemical properties in 1979 in EXP0 with those of EXP3, in which i_0 for snow was set to the default LIM2 value of zero. The results for modelled snow and ice volume were almost identical between the two experiments (Figure 13a), indicating a low sensitivity of these physical quantities to the change in i_0. On the other hand, an appreciable difference in the modelled bottom-ice PAR prior to the melt season in June results in a large difference in the modelled ice algal GPP (Figure 13b). By construction, the ice algal GPP in EXP3 is restricted to snow-free regions, so an increase in the ice algal GPP due to the change in i_0 reflects production in snow-covered regions (Figure 13c). The pan-Arctic ice algal annual GPP of EXP3 is 3.5 Tg C y^{-1}, only about a quarter of the value obtained in EXP0. The

Geosci. Model Dev. Discuss., https://doi.org/10.5194/gmd-2018-191
Manuscript under review for journal Geosci. Model Dev.
Discussion started: 23 August 2018

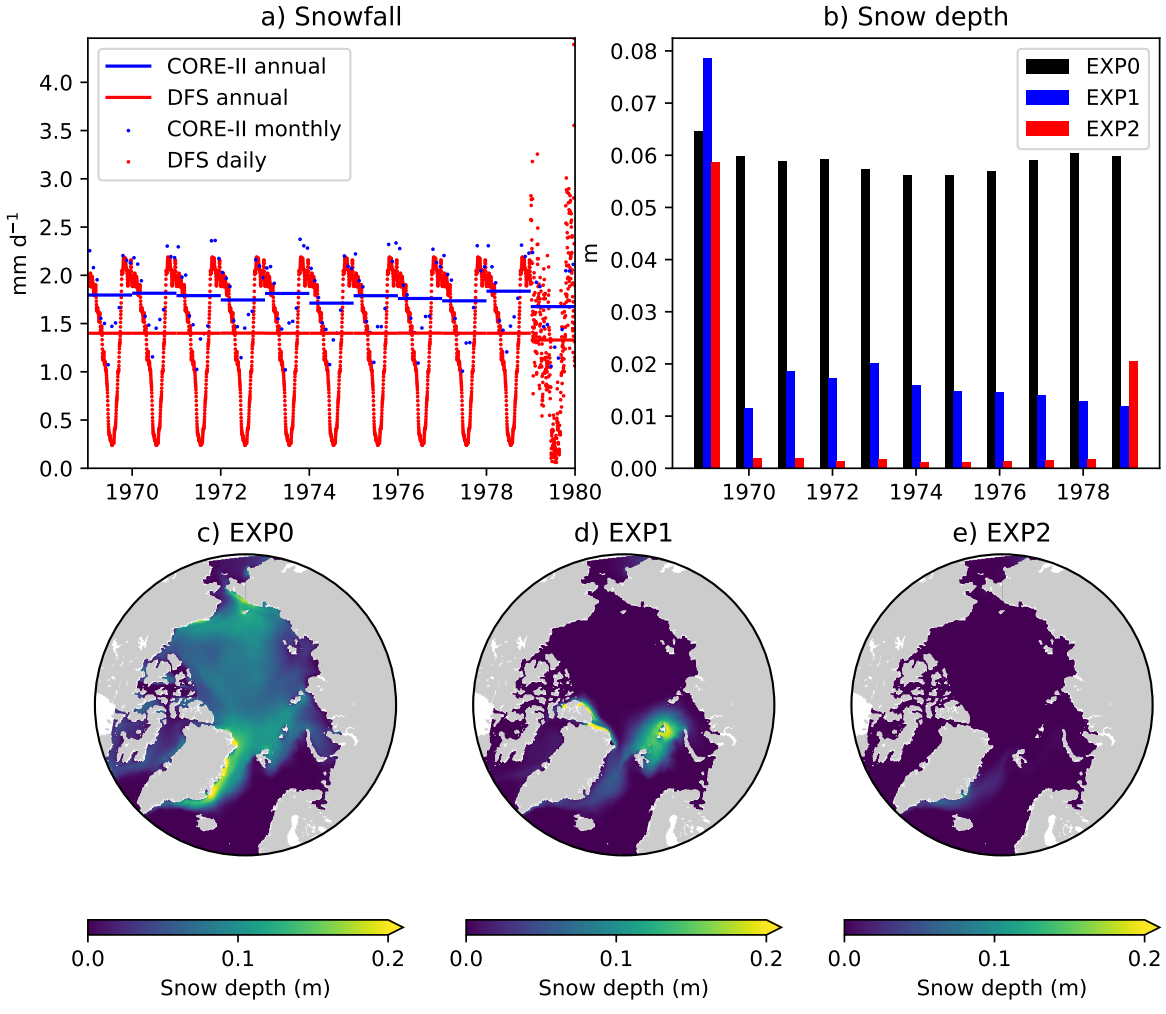

Figure 11. Model sensitivity to snowfall forcing frequency. Time series of pan-Arctic-mean a) prescribed snowfall rate of the CORE-II (blue) and DFS (red) datasets and b) modelled annual-mean snow depth in EXP0 (black), EXP1 (blue), and EXP2 (red). Spatial maps of modelled annual-mean snow depth for the period 1970-1978 in c) EXP0, d) EXP1, and e) EXP2. The units for the snowfall rate was converted from kg m^{-2} s^{-1} to mm d^{-1} using a constant snow density of 330 kg m^{-3}, which is the value assumed in LIM2.

Geosci. Model Dev. Discuss., https://doi.org/10.5194/gmd-2018-191
Manuscript under review for journal Geosci. Model Dev.
Discussion started: 23 August 2018

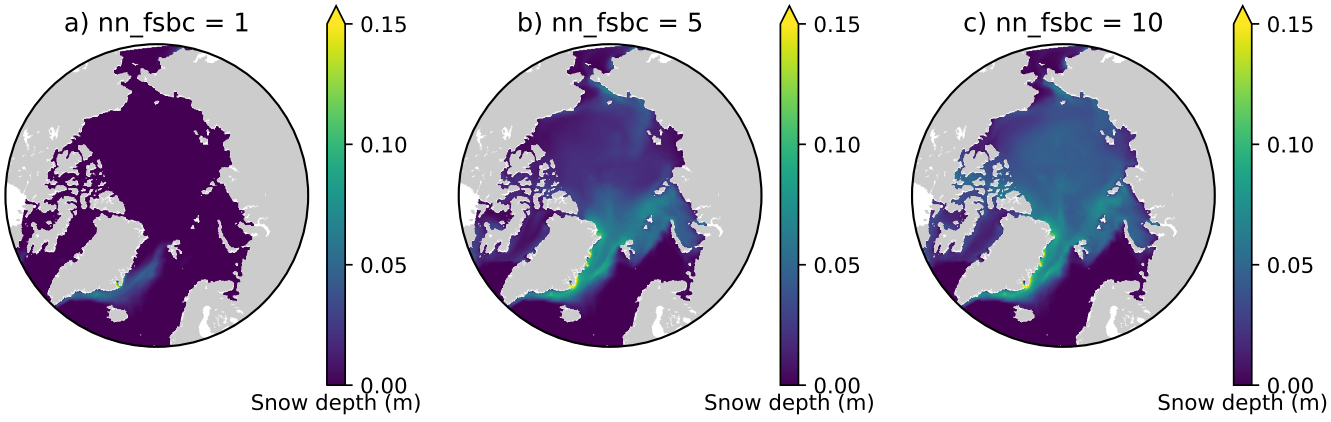

Figure 12. Sensitivity of modelled snow depth to the parameter nn_fsbc, which defines the frequency of the computation of surface boundary conditions and sea-ice physics relative to that of ocean dynamics. Spatial distribution of annual-mean modelled snow depth for year 1970 when nn_fsbc is set to a) 1, b) 5, and c) 10.

value is much lower than those of the previous studies (see Section 3.3.3). This result emphasizes the importance of correct representation of the light penetration through the snow column, and shows that the original LIM2 provides inadequate light for ice algal growth, resulting in insufficient pan-Arctic ice algal annual GPP. Note that the default value of i_0 is also set to zero in LIM3 (Vancoppenolle et al., 2012).

Previous 3D sea-ice biogeochemical models differed in their choices of values for i_0 (Table 1). The studies of Dupont (2012) and Jin et al. (2012) set this value to zero, yet their values for simulated ice algal productivity were relatively high. However, these models used special parametarizations for irradiance and light limitation, respectively, which likely resulted in realistic ice algal primary production values despite the impedence of light penetration through snow column. Dupont (2012) imposed a minimum lead fraction of 0.01 in any grid cell, supplying enough ambient light for ice algal growth. In Jin et al. (2012), the light limitation parameter (the ratio of light-limited slope and maximal photosynthetic rate; see Table 2 of Jin et al., 2006) was set to a very high value, nearly double the upper limit of the observed range reported in Table 2 of Lavoie et al. (2005). This reduction in light limitation allows the modelled ice algae to grow even under low light conditions.

Two other regional modelling studies prescribed non-zero values of i_0. Castellani et al. (2017) set i_0 to 0.3 based on the measurements over snow-free ice surface (Grenfell and Maykut, 1977). As such, this value should be viewed as an overestimate. Similarly, the light penetration through snow column was also overestimated in Watanabe et al. (2015), as i_0 was effectively unity in their study. Using these higher i_0 reduces light limitation, and hence enhances ice algal primary production.

To the best of the authors' knowledge, no studies have ever reported an observed value for i_0. For a snow-free ice surface, Grenfell and Maykut (1977) reported the values ranging between 0.18 and 0.63 depending on both the ice type and whether the incoming shortwave radiation is direct or diffuse. Observation-based estimates of i_0 would be useful in order to reduce the uncertainty of ice algal and under-ice phytoplankton growth in models.

Geosci. Model Dev. Discuss., https://doi.org/10.5194/gmd-2018-191
Manuscript under review for journal Geosci. Model Dev.
Discussion started: 23 August 2018

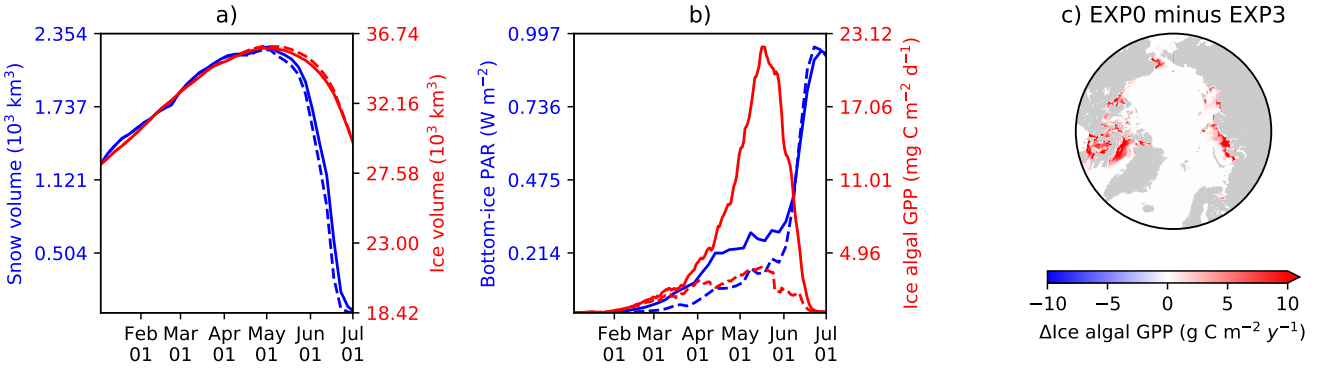

Figure 13. Model sensitivity to light penetration through snow. Time series comparison of modelled 5-day-mean a) snow volume (blue) and ice volume (red) and b) bottom-ice PAR (blue) and ice algal GPP (red) in 1979 between EXP0 (solid) and EXP3 (dashed). c) Spatial distribution of the difference in the ice algal annual GPP between EXP0 and EXP3.

4.3 Advection and eddy diffusion of sea-ice biogeochemical state variables (EXP4)

EXP4 was conducted with the identical model formulation as EXP0 except that the advection and eddy diffusion of sea-ice biogeochemical state variables were neglected. Note that the advection and diffusion of sea-ice physical state variables were retained in EXP4, and therefore, there is no change in the these variables between EXP0 and EXP4.

A time series comparison of the modelled pan-Arctic-mean bottom-ice nitrate and ice algal GPP for the year 1979 shows that these quantities are always higher in EXP0 than EXP4 (Figure 14a). The pan-Arctic annual-mean bottom-ice nitrate and the ice algal annual GPP are higher in EXP0 than EXP4 by 2 and 16 %, respectively. These results indicate that the overall effect of advection and eddy diffusion over the pan-Arctic is an increase in these quantites.

Although the overall effect is an enhancement, the spatial distribution shows regions of local increases and decreases (Figure 14c-d). The difference in nitrate concentration between the two experiments is relatively high off the west coast of Baffin Island, in which the bottom-ice nitrate is relatively high in EXP0 (Figure 14b), whereas the difference is relatively small in the Canadian Polar Shelf (Figure 14c). The difference in the spatial distribution of the ice algal GPP is relatively high in regions of high ice algal GPP except for the Canadian Polar Shelf (Figure 14d), which is a region of relatively slow ice motion (Figure 14e). A possible explanation for these spatial differences is that the horizontal transport within sea ice takes ice algae out of regions of high productivity into regions of low productivity, opening up space for new growth in the productive regions.

4.4 Shading of ice algae (EXP5)

In EXP5, the shading effect of ice algae on light transfer through the ice was neglected in order to assess its impact on under-ice NPP. On the pan-Arctic scale, there is almost no impact, as shown in Figure 15a. The differences in the pan-Arctic- and annual-mean under-ice PAR and the pan-Arctic under-ice annual NPP between EXP0 and EXP5 are only 2 % and 1 %, respectively.

Geosci. Model Dev. Discuss., https://doi.org/10.5194/gmd-2018-191
Manuscript under review for journal Geosci. Model Dev.
Discussion started: 23 August 2018

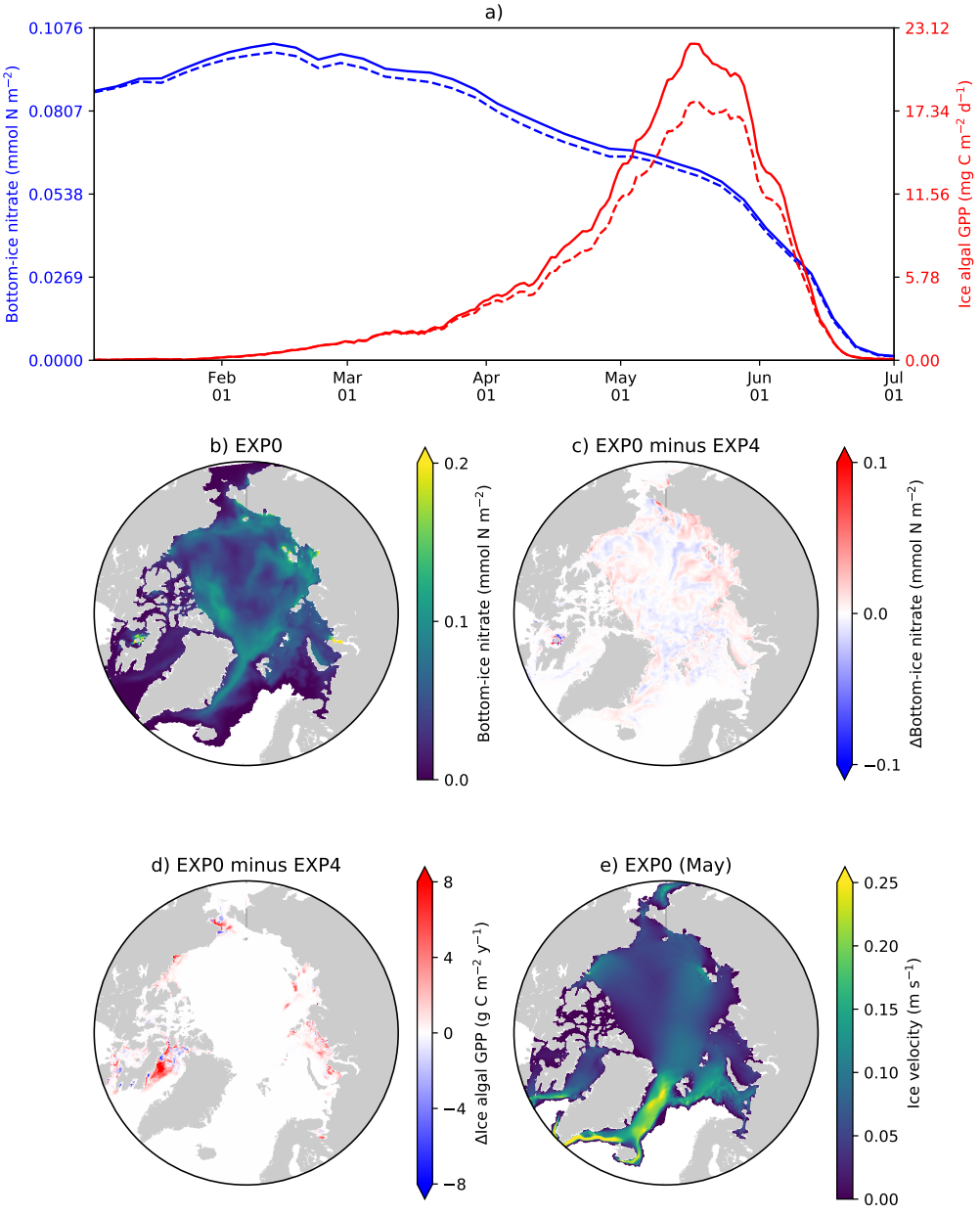

Figure 14. Model sensitivity to the advection and diffusion of sea-ice biogeochemical state variables. a) Time series comparison of 5-day- and pan-Arctic-mean modelled bottom-ice nitrate (blue) and ice algal daily GPP (red) during January-June of 1979 between EXP0 (solid) and EXP4 (dashed). Spatial maps of the annual-mean bottom-ice nitrate in b) EXP0 and c) its difference between EXP0 and EXP4, d) the difference in the ice algal annual GPP between EXP0 and EXP4, and e) the magnitude of the ice velocity during May.

Geosci. Model Dev. Discuss., https://doi.org/10.5194/gmd-2018-191
Manuscript under review for journal Geosci. Model Dev.
Discussion started: 23 August 2018

Consistent with the patchiness of the ice algal distribution (Figure 8c), the shading effect is rather localized as shown in Figure 15b-e. The influence on under-ice PAR is assessed for the month of the ice algal bloom peak (May; Figure 6c). By construction, the spatial distribution of the difference in the under-ice PAR between EXP0 and EXP5 is simply a reflection of ice algal abundance (Figure 15c). Similarly, a general decrease in the under-ice NPP is found due to shading in the regions of high modelled ice algae. However, in some regions, the shading results in a slight increase in the under-ice NPP. A possible explanation for this phenomenon is that the reduction in nutrient drawdown under regions of large ice algal biomass enchances nutrient advection into regions of low ice algal biomass.

The shading effect of ice algae was recently examined in the model study by Castellani et al. (2017). Their results showed that the effect has stronger influence at higher latitudes due to low ambient light. Furthermore, they hypothesized that the onset of the under-ice phytoplankton bloom north of 80°N can be delayed by up to 40 days depending on how their modelled under-ice PAR is affected by shading.

It is difficult to directly compare the results of the present study with those of Castellani et al. (2017) primarily due to the difference in the definition of the term under-ice. As described in Section 2.4.4, in the present study, a grid cell is considered "under-ice" as long as the ice concentration is 0.15 or above. Because of the strong light attenuation by snow and ice, the under-ice PAR defined in the present study is therefore dominated by the light through the open-water fraction. Consequently, the under-ice NPP is controlled by the light through the open-water fraction and does not show a strong influence by the shading of ice algae.

To carry out an analysis comparable to that of Castellani et al. (2017), we calculated the onset of under-ice phytoplankton bloom as follows. A bloom onset is defined as the day when bottom-ice PAR exceeds 0.4 W m^{-2} and remains above this value at least for 30 days. This threshold for bottom-ice PAR corresponds to the limit for under-ice algal growth considered in Castellani et al. (2017), assuming an unit conversion (from μmol photon m^{-2} s^{-1} to W m^{-2}) factor of 1/4.56 (Lavoie et al., 2005). Figure 16 shows the spatial variability in the under-ice bloom onset based on the definition above. The bloom took place mostly in seasonally ice-covered regions, while it was absent in most of the pack ice (as indicated by white regions). Unlike Castellani et al. (2017), the under-ice bloom north of 80°N was absent even without the shading effect. The absence of the bloom in our simulation is due to the presence of snow in this region; despite the extremely low quantity (< 0.01 m; data now shown), it kept the light level below the threshold for the bloom to occur. The median value of the onset is on the 155th day (June 6) when the shading is accounted (Figure 16a), while it is 10 days earlier without the shading effect (Figure 16b).

Figure 16c shows the spatial variability in the delay in the under-ice bloom onset caused by the ice algal shading. The values range from 5 to 275 days; in some places, the bloom is prevented completely. The present study does confirm the finding of Castellani et al. (2017) that the shading effect is spatially variable and can have a strong impact on the phytoplankton bloom under the ice of high ice algal biomass. However, given the patchiness of ice algal distribution and the control of the light through the open-water fraction, the impact of the shading on the estimate for the pan-Arctic under-ice annual NPP is negligible.

Geosci. Model Dev. Discuss., https://doi.org/10.5194/gmd-2018-191
Manuscript under review for journal Geosci. Model Dev.
Discussion started: 23 August 2018

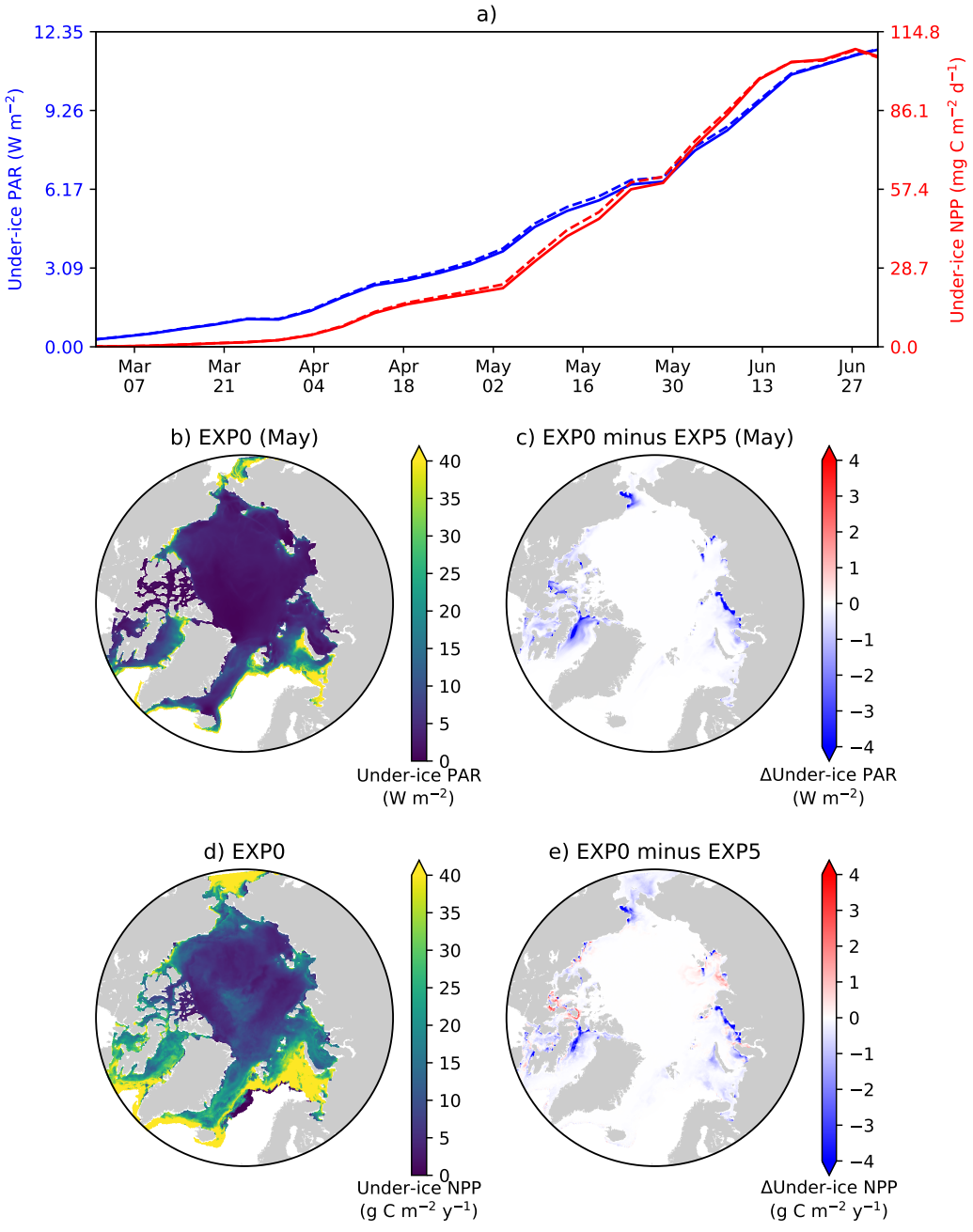

Figure 15. Model sensitivity to shading of ice algae. a) Time series comparison of modelled pan-Arctic- and 5-day-mean under-ice PAR (blue) and NPP (red) between EXP0 (solid) and EXP5 (dashed) during the year 1979. Spatial maps of b) the monthly-mean under-ice PAR in May in EXP0 and c) its difference from EXP5, d) the under-ice annual NPP in EXP0, and e) its difference from EXP5.

Geosci. Model Dev. Discuss., https://doi.org/10.5194/gmd-2018-191
Manuscript under review for journal Geosci. Model Dev.
Discussion started: 23 August 2018

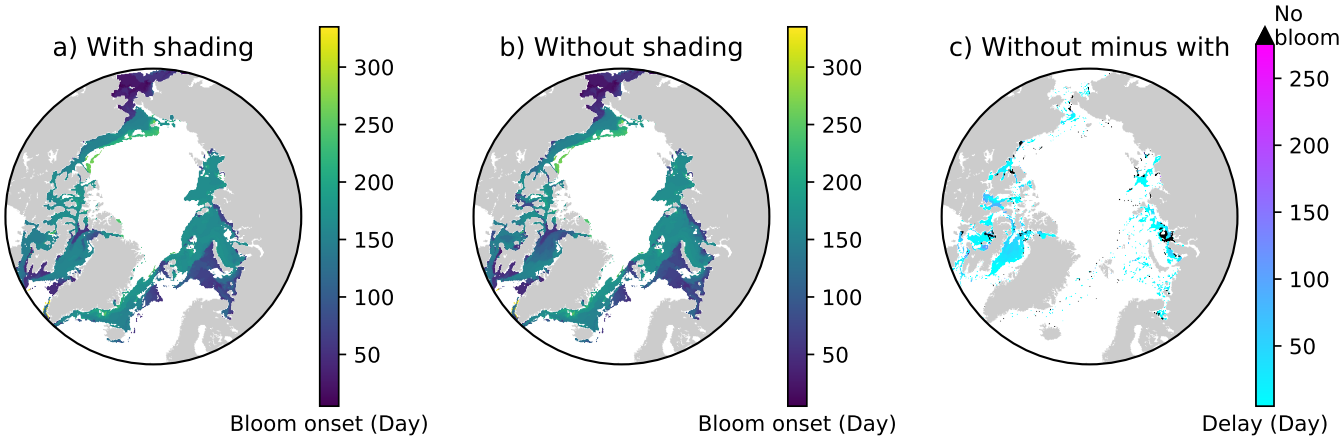

Figure 16. Effects of ice algal shading on the onset of under-ice phytoplankton bloom. Spatial maps showing the bloom onset (as the day from January 1) when the ice algal shading is a) considered and b) neglected and c) the difference between the two cases representing the delay due to the shading in 1979 in EXP0. In c), "No bloom" refers to regions in which the bloom was present in b) but not in a). See the main text for the definition of bloom onset.

5 Conclusions

In the present study, we have developed a sea-ice biogeochemical model which is coupled to NEMO. A number of modifications to the sea-ice physical model used in the standard distribution of NEMO (LIM2), to the ocean biogeochemical model (CanOE), and to the existing pan-Arctic configuration (NAA) were necessary to properly simulate the physical and biogeochemical processes in ice-covered regions. Results of the reference simulation (EXP0) agreed well with observations and previous studies in terms of simulated ice volume and extent and the pan-Arctic annual primary production of ice algae and phytoplankton. Adopting a high vertical resolution in the upper water column was found to be necessary to properly represent the effects of a meltwater lens on surface nutrients and the formation of a subsurface chlorophyll maximum. Furthermore, the vertical resolution was shown to have an effect on the magnitude of the modelled surface seawater DMS concentration (∼10 % annually and up to ∼20 % seasonally), which in turn influences DMS emissions. Results of the sensitivity experiments demonstrated that: LIM2 requires high-frequency (daily) snowfall forcing data to simulate realistic snow depth (EXP1 and 2); the assumption of no light penetration through snow in LIM2 is unrealistic for simulating an adequate ice algal bloom (EXP3); the advection and eddy diffusion of sea-ice biogeochemical state variables contributes to an enhancement of the pan-Arctic ice algal annual GPP by 16 % (EXP4); and attenuation of light by ice algae has local influence on under-ice NPP but is negligible when estimating larger-scale quantities (e.g. pan-Arctic under-ice annual NPP) (EXP5). The modifications to LIM2, CanOE, and NAA adopted in the present study are also applicable to other submodels and configurations of NEMO (e.g. LIM3, PISCES, and ORCA, respectively) as the code structures are similar, and therefore, can be incorporated into future pan-Arctic biogeochemical studies. The sea-ice biogeochemical model developed in the present study has been embedded into NEMO in

a generic way (see Appendix A), and can therefore be easily coupled to the aforementioned submodels. To our knowledge, such a development has not been done previously within NEMO. Further sensitivity experiments and observational constraints are needed to refine the important parameters (e.g. i_0) for sea-ice biogeochemistry.

Code availability. The model code and the configuration used for conducting model simulations are available for download at www.gitlab.com/hakasehayashida/canoe-dms/tree/version1.

Appendix A: Implementation of ocean sulfur cycle and sea-ice biogeochemistry into the NEMO source code

Figure A1 shows the structure of the NEMO v3.4 source code directory (NEMO), which includes the following subdirectories (submodels): OPA_SRC (OPA), LIM_SRC_2 (LIM2), and TOP_SRC (ocean biogeochemistry). The directory TOP_SRC contains two subdirectories: PISCES and MY_TRC. In this study, the directory PISCES contains the source code of CanOE, as CanOE has been developed using the code structure of the PISCES ocean biogeochemical model. The other directory, MY_TRC, consists of a list of generic modules that can be modified by end users to add their own biogeochemical models; we introduced an ocean sulfur cycle and sea-ice biogeochemistry into this interface. Furthermore, we modified a few modules in the directories LIM_SRC_2 and PISCES for the implementation of sea-ice biogeochemistry into the NEMO modelling system (Table A1).

Numerically, the tendencies for the sea-ice biogeochemical state variables are computed at each time step as follows: first, the concentrations of all state variables from the previous time step are transferred from the module trcsms_my_trc.F90 to the module limtrp_2.F90 to compute the advective and diffusive tendencies. The updated concentrations are transferred back to the module trcsms_my_trc.F90 within which the biological and chemical sources and sinks as well as the ice-ocean fluxes of these state variables are computed.

In NEMO, user-specific modules built within MY_TRC are designed to be activated by defining the C preprocessor (CPP) key key_my_trc. As such, we assigned CPP keys for each component of the newly-developed models, which can be activated as needed (Table A2).

Competing interests. The authors declare that they have no conflict of interest.

Acknowledgements. This study contributes to the SCOR Working group on Biogeochemical Exchange Processes at Sea Ice Interfaces (BEPSII), the Network on Climate and Aerosols: Addressing Key Uncertainties in Remote Canadian Environments (NETCARE), and ArcticNet. We acknowledge funding from NETCARE, ArcticNet, Fisheries and Oceans Canada, and Environment and Climate Change Canada. This research was enabled in part by support provided by WestGrid (www.westgrid.ca) and Compute Canada (www.computecanada.ca). We thank Belaid Moa (University of Victoria) for computational support, Arlan Dirkson (Université du Québec à Montréal) for providing a netCDF

Geosci. Model Dev. Discuss., https://doi.org/10.5194/gmd-2018-191
Manuscript under review for journal Geosci. Model Dev.
Discussion started: 23 August 2018

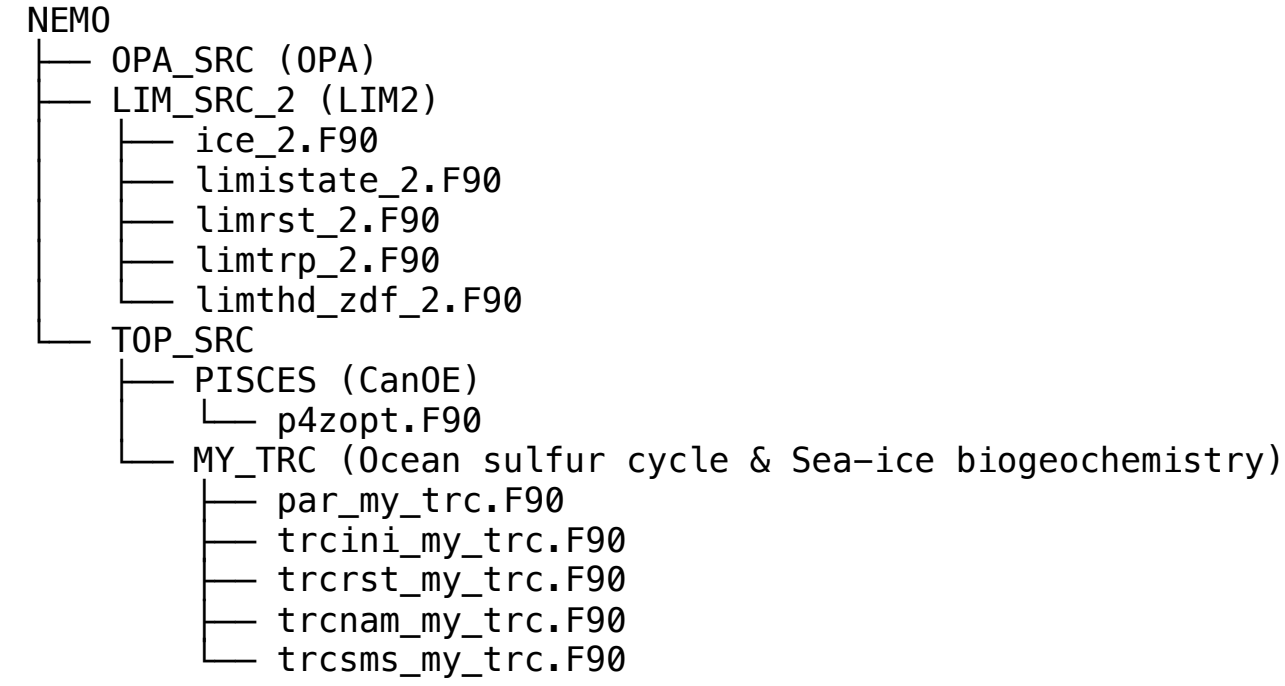

Figure A1. File tree diagram of the OPA-LIM2-CanOE configuration of NEMO v3.4. The modules listed in the diagram (*.F90) have been modified in order to implement ocean sulfur cycle and sea-ice biogeochemistry into the present configuration.

Table A1. A list of NEMO modules modified to add ocean sulfur cycle and sea-ice biogeochemistry.

Module	Description of the modification
ice_2.F90	Assign arrays for advective and diffusive tendencies of the sea-ice biogeochemical state variables.
limistate_2.F90	Initialize the arrays for the advective and diffusive tendencies.
limrst_2.F90	Restart the arrays for the advective and diffusive tendencies.
limtrp_2.F90	Compute the advective and diffusive tendencies as described in Section 2.3.1.
limthd_zdf_2.F90	Compute the light penetration parameterization through snow and sea ice as described in Section 2.1.
p4zopt.F90	Compute ice-algal shading and under-ice PAR as described in Section 2.2.2.
par_my_trc.F90	Define the number of state and diagnostic variables.
trcini_my_trc.F90	Initialize the state variables.
trcrst_my_trc.F90	Restart the state variables.
trcnam_my_trc.F90	Assign the arrays of the state and diagnostic variables.
trcsms_my_trc.F90	Compute the biological and chemical sources and sinks and ice-ocean fluxes.

version of the PIOMAS monthly-mean ice thickness and concentration gridded data products, and Clark Pennelly (University of Alberta) for

Geosci. Model Dev. Discuss., https://doi.org/10.5194/gmd-2018-191
Manuscript under review for journal Geosci. Model Dev.
Discussion started: 23 August 2018

Table A2. A list of CPP keys created in the present study.

CPP key	Description
key_my_trc_ocedms	Activate ocean sulfur cycle.
key_my_trc_iceeco	Activate sea-ice ecosystem.
key_my_trc_icedms	Activate sea-ice sulfur cycle.

providing a modified version of the DFS dataset. The original NAA configuration was developed under an NSERC Discovery Grant award to PGM.

References

Abraham, C., Steiner, N., Monahan, A., and Michel, C.: Effects of subgrid-scale snow thickness variability on radiative transfer in sea ice, Journal of Geophysical Research: Oceans, 120, 5597–5614, https://doi.org/10.1002/2015JC010741, 2015.

Amante, C. and Eakins, B. W.: ETOPO1 1 arc-minute global relief model: procedures, data sources and analysis, US Department of Commerce, National Oceanic and Atmospheric Administration, National Environmental Satellite, Data, and Information Service, National Geophysical Data Center, Marine Geology and Geophysics Division Colorado, 2009.

Arora, V. K., Scinocca, J. F., Boer, G. J., Christian, J. R., Denman, K. L., Flato, G. M., Kharin, V. V., Lee, W. G., and Merryfield, W. J.: Carbon emission limits required to satisfy future representative concentration pathways of greenhouse gases, Geophysical Research Letters, 38, https://doi.org/10.1029/2010GL046270, 2011.

Arrigo, K. R.: Sea Ice Ecosystems, Annual Review of Marine Science, 6, 439–467, https://doi.org/10.1146/annurev-marine-010213-135103, 2014.

Arrigo, K. R., Sullivan, C. W., and Kremer, J. N.: A bio-optical model of Antarctic sea ice, Journal of Geophysical Research: Oceans, 96, 10 581–10 592, https://doi.org/10.1029/91JC00455, 1991.

Aumont, O., Ethé, C., Tagliabue, A., Bopp, L., and Gehlen, M.: PISCES-v2: an ocean biogeochemical model for carbon and ecosystem studies, Geoscientific Model Development, 8, 2465–2513, https://doi.org/10.5194/gmd-8-2465-2015, 2015.

Balmaseda, M. A., Mogensen, K., and Weaver, A. T.: Evaluation of the ECMWF ocean reanalysis system ORAS4, Quarterly Journal of the Royal Meteorological Society, 139, 1132–1161, https://doi.org/10.1002/qj.2063, 2013.

Bouillon, S., Maqueda, M. A. M., Legat, V., and Fichefet, T.: An elastic–viscous–plastic sea ice model formulated on Arakawa B and C grids, Ocean Modelling, 27, 174–184, 2009.

Castellani, G., Losch, M., Lange, B. A., and Flores, H.: Modeling Arctic sea-ice algae: Physical drivers of spatial distribution and algae phenology, Journal of Geophysical Research: Oceans, 122, 7466–7487, https://doi.org/10.1002/2017JC012828, 2017.

Dai, A. and Trenberth, K. E.: Estimates of Freshwater Discharge from Continents: Latitudinal and Seasonal Variations, Journal of Hydrometeorology, 3, 660–687, https://doi.org/10.1175/1525-7541(2002)003<0660:EOFDFC>2.0.CO;2, 2002.

Deal, C., Jin, M., Elliott, S., Hunke, E., Maltrud, M., and Jeffery, N.: Large-scale modeling of primary production and ice algal biomass within arctic sea ice in 1992, Journal of Geophysical Research, 116, https://doi.org/10.1029/2010JC006409, 2011.

Dee, D. P., Uppala, S. M., Simmons, A. J., Berrisford, P., Poli, P., Kobayashi, S., Andrae, U., Balmaseda, M. A., Balsamo, G., Bauer, P., Bechtold, P., Beljaars, A. C. M., van de Berg, L., Bidlot, J., Bormann, N., Delsol, C., Dragani, R., Fuentes, M., Geer, A. J., Haimberger, L., Healy, S. B., Hersbach, H., Hólm, E. V., Isaksen, L., Kållberg, P., Köhler, M., Matricardi, M., McNally, A. P., Monge-Sanz, B. M., Morcrette, J.-J., Park, B.-K., Peubey, C., de Rosnay, P., Tavolato, C., Thépaut, J.-N., and Vitart, F.: The ERA-Interim reanalysis: configuration and performance of the data assimilation system, Quarterly Journal of the Royal Meteorological Society, 137, 553–597, https://doi.org/10.1002/qj.828, 2011.

Dirkson, A., Merryfield, W. J., and Monahan, A.: Impacts of Sea Ice Thickness Initialization on Seasonal Arctic Sea Ice Predictions, Journal of Climate, 30, 1001–1017, https://doi.org/10.1175/JCLI-D-16-0437.1, 2016.

Dupont, F.: Impact of sea-ice biology on overall primary production in a biophysical model of the pan-Arctic Ocean, Journal of Geophysical Research: Oceans, 117, C00D17, https://doi.org/10.1029/2011JC006983, 2012.

Dupont, F., Higginson, S., Bourdallé-Badie, R., Lu, Y., Roy, F., Smith, G. C., Lemieux, J.-F., Garric, G., and Davidson, F.: A high-resolution ocean and sea-ice modelling system for the Arctic and North Atlantic oceans, Geosci. Model Dev., 8, 1577–1594, https://doi.org/10.5194/gmd-8-1577-2015, 2015.

Dussin, R., Barnier, B., Brodeau, L., and Molines, J. M.: DRAKKAR FORCING SET DFS5, 2016.

Fichefet, T. and Maqueda, M. A. M.: Sensitivity of a global sea ice model to the treatment of ice thermodynamics and dynamics, Journal of Geophysical Research: Oceans, 102, 12 609–12 646, https://doi.org/10.1029/97JC00480, 1997.

Flato, G. M. and Brown, R. D.: Variability and climate sensitivity of landfast Arctic sea ice, Journal of Geophysical Research: Oceans, 101, 25 767–25 777, https://doi.org/10.1029/96JC02431, 1996.

Garcia, H. E., Locarnini, R. A., Boyer, T. P., Antonov, J. I., Baranova, O. K., Zweng, M. M., Reagan, J. R., and Johnson, D. R.: World Ocean Atlas 2013, Volume 3: Dissolved Oxygen, Apparent Oxygen Utilization, and Oxygen Saturation, s. Levitus, Ed., A. Mishonov Technical Ed.; NOAA Atlas NESDIS 75, 27 pp., 2014.

Gosselin, M., Levasseur, M., Wheeler, P. A., Horner, R. A., and Booth, B. C.: New measurements of phytoplankton and ice algal production in the Arctic Ocean, Deep Sea Research Part II: Topical Studies in Oceanography, 44, 1623–1644, 1997.

Grenfell, T. C. and Maykut, G. A.: The optical properties of ice and snow in the Arctic Basin, Journal of Glaciology, 18, 445–463, 1977.

Hayashida, H., Steiner, N., Monahan, A., Galindo, V., Lizotte, M., and Levasseur, M.: Implications of sea-ice biogeochemistry for oceanic production and emissions of dimethyl sulfide in the Arctic, Biogeosciences, 14, 3129–3155, https://doi.org/10.5194/bg-14-3129-2017, 2017.

Hu, X. and Myers, P. G.: A Lagrangian view of Pacific water inflow pathways in the Arctic Ocean during model spin-up, Ocean Modelling, 71, 66–80, https://doi.org/10.1016/j.ocemod.2013.06.007, 2013.

Hu, X. and Myers, P. G.: Changes to the Canadian Arctic Archipelago Sea Ice and Freshwater Fluxes in the Twenty-First Century under the Intergovernmental Panel on Climate Change A1B Climate Scenario, Atmosphere-Ocean, 52, 331–350, https://doi.org/10.1080/07055900.2014.942592, 2014.

Jin, M., Deal, C. J., Wang, J., Shin, K.-H., Tanaka, N., Whitledge, T. E., Lee, S. H., and Gradinger, R. R.: Controls of the landfast ice–ocean ecosystem offshore Barrow, Alaska, Annals of Glaciology, 44, 63–72, 2006.

Jin, M., Deal, C., Lee, S. H., Elliott, S., Hunke, E., Maltrud, M., and Jeffery, N.: Investigation of Arctic sea ice and ocean primary production for the period 1992–2007 using a 3-D global ice–ocean ecosystem model, Deep Sea Research Part II: Topical Studies in Oceanography, 81–84, 28–35, https://doi.org/10.1016/j.dsr2.2011.06.003, 2012.

Jin, M., Popova, E. E., Zhang, J., Ji, R., Pendleton, D., Varpe, \., Yool, A., and Lee, Y. J.: Ecosystem model intercomparison of under-ice and total primary production in the Arctic Ocean, Journal of Geophysical Research: Oceans, pp. n/a–n/a, https://doi.org/10.1002/2015JC011183, 2015.

Jin, M., Deal, C., Maslowski, W., Matrai, P., Roberts, A., Osinski, R., Lee, Y. J., Frants, M., Elliott, S., Jeffery, N., Hunke, E., and Wang, S.: Effects of Model Resolution and Ocean Mixing on Forced Ice-Ocean Physical and Biogeochemical Simulations Using Global and Regional System Models, Journal of Geophysical Research: Oceans, https://doi.org/10.1002/2017JC013365, 2018.

Lauvset, S. K., Key, R. M., Olsen, A., van Heuven, S., Velo, A., Lin, X., Schirnick, C., Kozyr, A., Tanhua, T., Hoppema, M., Jutterström, S., Steinfeldt, R., Jeansson, E., Ishii, M., Perez, F. F., Suzuki, T., and Watelet, S.: A new global interior ocean mapped climatology: the 1° × 1° GLODAP version 2, Earth System Science Data, 8, 325–340, https://doi.org/10.5194/essd-8-325-2016, 2016.

Lavoie, D., Denman, K., and Michel, C.: Modeling ice algal growth and decline in a seasonally ice-covered region of the Arctic (Resolute Passage, Canadian Archipelago), Journal of Geophysical Research, 110, C11 009, https://doi.org/10.1029/2005JC002922, 2005.

Legendre, L., Ackley, S. F., Dieckmann, G. S., Gulliksen, B., Horner, R., Hoshiai, T., Melnikov, I. A., Reeburgh, W. S., Spindler, M., and Sullivan, C. W.: Ecology of sea ice biota, Polar Biology, 12, 429–444, https://doi.org/10.1007/BF00243114, 1992.

Leu, E., Mundy, C. J., Assmy, P., Campbell, K., Gabrielsen, T. M., Gosselin, M., Juul-Pedersen, T., and Gradinger, R.: Arctic spring awakening – Steering principles behind the phenology of vernal ice algal blooms, Progress in Oceanography, 139, 151–170, https://doi.org/10.1016/j.pocean.2015.07.012, 2015.

Loose, B., McGillis, W. R., Schlosser, P., Perovich, D., and Takahashi, T.: Effects of freezing, growth, and ice cover on gas transport processes in laboratory seawater experiments, Geophysical Research Letters, 36, L05 603, https://doi.org/10.1029/2008GL036318, 2009.

Madec, G.: NEMO ocean engine, Tech. Rep. 27, Institut Pierre Simon Laplace (ISPL), 2008.

Maykut, G. A. and Untersteiner, N.: Some results from a time-dependent thermodynamic model of sea ice, Journal of Geophysical Research, 76, 1550–1575, https://doi.org/10.1029/JC076i006p01550, 1971.

Miller, L. A., Fripiat, F., Else, B. G., Bowman, J. S., Brown, K. A., Collins, R. E., Ewert, M., Fransson, A., Gosselin, M., Lannuzel, D., Meiners, K. M., Michel, C., Nishioka, J., Nomura, D., Papadimitriou, S., Russell, L. M., Sørensen, L. L., Thomas, D. N., Tison, J.-L., van Leeuwe, M. A., Vancoppenolle, M., Wolff, E. W., and Zhou, J.: Methods for biogeochemical studies of sea ice: The state of the art, caveats, and recommendations, Elementa: Science of the Anthropocene, 3, 000 038, https://doi.org/10.12952/journal.elementa.000038, 2015.

Morel, A.: Optical modeling of the upper ocean in relation to its biogenous matter content (case I waters), Journal of Geophysical Research: Oceans, 93, 10 749–10 768, https://doi.org/10.1029/JC093iC09p10749, 1988.

Mortenson, E., Hayashida, H., Steiner, N., Monahan, A., Blais, M., Gale, M. A., Galindo, V., Gosselin, M., Hu, X., Lavoie, D., and Mundy, C. J.: A model-based analysis of physical and biological controls on ice algal and pelagic primary production in Resolute Passage, Elem Sci Anth, 5, https://doi.org/10.1525/elementa.229, 2017.

Pabi, S., van Dijken, G. L., and Arrigo, K. R.: Primary production in the Arctic Ocean, 1998–2006, Journal of Geophysical Research: Oceans, 113, C08 005, https://doi.org/10.1029/2007JC004578, 2008.

Popova, E. E., Yool, A., Coward, A. C., Dupont, F., Deal, C., Elliott, S., Hunke, E., Jin, M., Steele, M., and Zhang, J.: What controls primary production in the Arctic Ocean? Results from an intercomparison of five general circulation models with biogeochemistry, Journal of Geophysical Research: Oceans, 117, C00D12, https://doi.org/10.1029/2011JC007112, 2012.

Prather, M. J.: Numerical advection by conservation of second-order moments, Journal of Geophysical Research: Atmospheres, 91, 6671–6681, https://doi.org/10.1029/JD091iD06p06671, 1986.

Sakshaug, E.: Primary and Secondary Production in the Arctic Seas, in: The Organic Carbon Cycle in the Arctic Ocean, edited by Stein, R. and MacDonald, R. W., pp. 57–81, Springer Berlin Heidelberg, https://doi.org/10.1007/978-3-642-18912-8_3, 2004.

Schweiger, A., Lindsay, R., Zhang, J., Steele, M., Stern, H., and Kwok, R.: Uncertainty in modeled Arctic sea ice volume, Journal of Geophysical Research: Oceans, 116, C00D06, https://doi.org/10.1029/2011JC007084, 2011.

Stefels, J., Steinke, M., Turner, S., Malin, G., and Belviso, S.: Environmental constraints on the production and removal of the climatically active gas dimethylsulphide (DMS) and implications for ecosystem modelling, Biogeochemistry, 83, 245–275, https://doi.org/10.1007/s10533-007-9091-5, 2007.

Steiner, N. S., Sou, T., Deal, C., Jackson, J. M., Jin, M., Popova, E., Williams, W., and Yool, A.: The Future of the Subsurface Chlorophyll-a Maximum in the Canada Basin - A Model Intercomparison, Journal of Geophysical Research: Oceans, 120, 23, https://doi.org/10.1002/2015JC011232, 2015.

Tedesco, L., Miettunen, E., An, B. W., Happala, J., and Kaartokallio, H.: Long-term mesoscale variability of modelled sea-ice primary production in the northern Baltic Sea, Elem Sci Anth, 5, https://doi.org/10.1525/elementa.223, 2017.

Uppala, S. M., KÅllberg, P. W., Simmons, A. J., Andrae, U., Bechtold, V. D. C., Fiorino, M., Gibson, J. K., Haseler, J., Hernandez, A., Kelly, G. A., Li, X., Onogi, K., Saarinen, S., Sokka, N., Allan, R. P., Andersson, E., Arpe, K., Balmaseda, M. A., Beljaars, A. C. M., Berg, L. V. D., Bidlot, J., Bormann, N., Caires, S., Chevallier, F., Dethof, A., Dragosavac, M., Fisher, M., Fuentes, M., Hagemann, S., Hólm, E., Hoskins, B. J., Isaksen, L., Janssen, P. a. E. M., Jenne, R., Mcnally, A. P., Mahfouf, J.-F., Morcrette, J.-J., Rayner, N. A., Saunders, R. W., Simon, P., Sterl, A., Trenberth, K. E., Untch, A., Vasiljevic, D., Viterbo, P., and Woollen, J.: The ERA-40 re-analysis, Quarterly Journal of the Royal Meteorological Society, 131, 2961–3012, https://doi.org/10.1256/qj.04.176, 2005.

Vancoppenolle, M. and Tedesco, L.: Numerical models of sea ice biogeochemistry, in: Sea Ice, pp. 492–515, Wiley-Blackwell, 3 edn., https://doi.org/10.1002/9781118778371.ch20, 2016.

Vancoppenolle, M., Goosse, H., de Montety, A., Fichefet, T., Tremblay, B., and Tison, J.-L.: Modeling brine and nutrient dynamics in Antarctic sea ice: The case of dissolved silica, Journal of Geophysical Research, 115, https://doi.org/10.1029/2009JC005369, 2010.

Vancoppenolle, M., Bouillon, S., Fichefet, T., Goosse, H., Lecomte, O., Maqueda, M. A. M., and Madec, G.: The Louvain-la-Neuve sea ice model, Tech. rep., Tech. rep., Université catholique de Louvain, 2012.

Vancoppenolle, M., Meiners, K. M., Michel, C., Bopp, L., Brabant, F., Carnat, G., Delille, B., Lannuzel, D., Madec, G., Moreau, S., Tison, J.-L., and van der Merwe, P.: Role of sea ice in global biogeochemical cycles: emerging views and challenges, Quaternary Science Reviews, 79, 207–230, https://doi.org/10.1016/j.quascirev.2013.04.011, 2013.

Warren, S. G., Rigor, I. G., Untersteiner, N., Radionov, V. F., Bryazgin, N. N., Aleksandrov, Y. I., and Colony, R.: Snow Depth on Arctic Sea Ice, Journal of Climate, 12, 1814–1829, https://doi.org/10.1175/1520-0442, 1999.

Watanabe, E.: Linkages among halocline variability, shelf-basin interaction, and wind regimes in the Beaufort Sea demonstrated in pan-Arctic Ocean modeling framework, Ocean Modelling, 71, 43–53, https://doi.org/10.1016/j.ocemod.2012.12.010, 2013.

Watanabe, E., Onodera, J., Harada, N., Aita, M. N., Ishida, A., and Kishi, M. J.: Wind-driven interannual variability of sea ice algal production in the western Arctic Chukchi Borderland, Biogeosciences, 12, 6147–6168, https://doi.org/10.5194/bg-12-6147-2015, 2015.

Windnagel, A., Brandt, M., Fetterer, F., and Meier, W.: Sea Ice Index Version 3 Analysis, NSIDC Special Report 19, 2017.

Wolf-Gladrow, D. A., Zeebe, R. E., Klaas, C., Körtzinger, A., and Dickson, A. G.: Total alkalinity: The explicit conservative expression and its application to biogeochemical processes, Marine Chemistry, 106, 287–300, https://doi.org/10.1016/j.marchem.2007.01.006, 2007.

Zeebe, R. E., Eicken, H., Robinson, D. H., Wolf-Gladrow, D., and Dieckmann, G. S.: Modeling the heating and melting of sea ice through light absorption by microalgae, Journal of Geophysical Research: Oceans, 101, 1163–1181, https://doi.org/10.1029/95JC02687, 1996.

Zhang, J. and Rothrock, D. A.: Modeling Global Sea Ice with a Thickness and Enthalpy Distribution Model in Generalized Curvilinear Coordinates, Monthly Weather Review, 131, 845–861, https://doi.org/10.1175/1520-0493(2003)131<0845:MGSIWA>2.0.CO;2, 2003.

Zhang, J., Spitz, Y. H., Steele, M., Ashjian, C., Campbell, R., Berline, L., and Matrai, P.: Modeling the impact of declining sea ice on the Arctic marine planktonic ecosystem, Journal of Geophysical Research: Oceans, 115, C10 015, https://doi.org/10.1029/2009JC005387, 2010.